



# DIGITAL ACCESS TO SCHOLARSHIP AT HARVARD

## Galaxy clusters discovered via the Sunyaev-Zel'dovich effect in the first 720 square degrees of the South Pole Telescope survey

The Harvard community has made this article openly available.  
[Please share](#) how this access benefits you. Your story matters.

<b>Citation</b>	Reichardt, C. L., B. Stalder, L. E. Bleem, T. E. Montroy, K. A. Aird, K. Andersson, R. Armstrong, et al. 2013. "Galaxy clusters discovered via the Sunyaev-Zel'dovich effect in the first 720 square degrees of the South Pole Telescope survey." <i>The Astrophysical Journal</i> 763 (2) (February 1): 127. doi:10.1088/0004-637x/763/2/127. <a href="http://dx.doi.org/10.1088/0004-637X/763/2/127">http://dx.doi.org/10.1088/0004-637X/763/2/127</a> .
<b>Published Version</b>	<a href="https://doi.org/10.1088/0004-637X/763/2/127">doi:10.1088/0004-637X/763/2/127</a>
<b>Accessed</b>	April 17, 2018 4:28:22 PM EDT
<b>Citable Link</b>	<a href="http://nrs.harvard.edu/urn-3:HUL.InstRepos:11829465">http://nrs.harvard.edu/urn-3:HUL.InstRepos:11829465</a>
<b>Terms of Use</b>	This article was downloaded from Harvard University's DASH repository, and is made available under the terms and conditions applicable to Other Posted Material, as set forth at <a href="http://nrs.harvard.edu/urn-3:HUL.InstRepos:dash.current.terms-of-use#LAA">http://nrs.harvard.edu/urn-3:HUL.InstRepos:dash.current.terms-of-use#LAA</a>

*(Article begins on next page)*

## GALAXY CLUSTERS DISCOVERED VIA THE SUNYAEV-ZEL'DOVICH EFFECT IN THE FIRST 720 SQUARE DEGREES OF THE SOUTH POLE TELESCOPE SURVEY

C. L. REICHARDT<sup>1</sup>, B. STALDER<sup>2</sup>, L. E. BLEEM<sup>3,4</sup>, T. E. MONTROY<sup>5</sup>, K. A. AIRD<sup>6</sup>, K. ANDERSSON<sup>7,8</sup>, R. ARMSTRONG<sup>9</sup>, M. L. N. ASHBY<sup>2</sup>, M. BAUTZ<sup>8</sup>, M. BAYLISS<sup>10</sup>, G. BAZIN<sup>7,11</sup>, B. A. BENSON<sup>3,12</sup>, M. BRODWIN<sup>13</sup>, J. E. CARLSTROM<sup>3,4,12,14,15</sup>, C. L. CHANG<sup>3,12,13</sup>, H. M. CHO<sup>16</sup>, A. CLOCCHIATTI<sup>17</sup>, T. M. CRAWFORD<sup>3,14</sup>, A. T. CRITES<sup>3,14</sup>, T. DE HAAN<sup>18</sup>, S. DESAI<sup>7,11</sup>, M. A. DOBBS<sup>18</sup>, J. P. DUDLEY<sup>18</sup>, R. J. FOLEY<sup>2</sup>, W. R. FORMAN<sup>2</sup>, E. M. GEORGE<sup>1</sup>, M. D. GLADDERS<sup>3,14</sup>, A. H. GONZALEZ<sup>19</sup>, N. W. HALVERSON<sup>20</sup>, N. L. HARRINGTON<sup>1</sup>, F. W. HIGH<sup>3,14</sup>, G. P. HOLDER<sup>18</sup>, W. L. HOLZAPFEL<sup>1</sup>, S. HOOVER<sup>3,12</sup>, J. D. HRUBES<sup>6</sup>, C. JONES<sup>2</sup>, M. JOY<sup>21</sup>, R. KEISLER<sup>3,4</sup>, L. KNOX<sup>22</sup>, A. T. LEE<sup>1,23</sup>, E. M. LEITCH<sup>3,14</sup>, J. LIU<sup>7,11</sup>, M. LUEKER<sup>1,24</sup>, D. LUONG-VAN<sup>6</sup>, A. MANTZ<sup>3</sup>, D. P. MARRONE<sup>25</sup>, M. McDONALD<sup>8</sup>, J. J. MCMAHON<sup>3,12,26</sup>, J. MEHL<sup>3,14</sup>, S. S. MEYER<sup>3,4,12,14</sup>, L. MOCANU<sup>3,14</sup>, J. J. MOHR<sup>7,11,27</sup>, S. S. MURRAY<sup>2</sup>, T. NATOLI<sup>3,4</sup>, S. PADIN<sup>3,14,24</sup>, T. PLAGGE<sup>3,14</sup>, C. PRYKE<sup>28</sup>, A. REST<sup>29</sup>, J. RUEL<sup>10</sup>, J. E. RUHL<sup>5</sup>, B. R. SALIWANCHIK<sup>5</sup>, A. SARO<sup>7</sup>, J. T. SAYRE<sup>5</sup>, K. K. SCHAFFER<sup>3,12,30</sup>, L. SHAW<sup>18,31</sup>, E. SHIROKOFF<sup>1,24</sup>, J. SONG<sup>26</sup>, H. G. SPIELER<sup>23</sup>, Z. STANISZEWSKI<sup>5</sup>, A. A. STARK<sup>2</sup>, K. STORY<sup>3,4</sup>, C. W. STUBBS<sup>2,10</sup>, R. ŠUHADA<sup>7</sup>, A. VAN ENGELEN<sup>18</sup>, K. VANDERLINDE<sup>18</sup>, J. D. VIEIRA<sup>3,4,24</sup>, A. VIKHLININ<sup>2</sup>, R. WILLIAMSON<sup>3,14</sup>, O. ZAHN<sup>1,32</sup>, AND A. ZENTENO<sup>7,11</sup>

*Draft version March 27, 2012*

### ABSTRACT

We present a catalog of 224 galaxy cluster candidates, selected through their Sunyaev-Zel'dovich (SZ) effect signature in the first 720 deg<sup>2</sup> of the South Pole Telescope (SPT) survey. This area was mapped with the SPT in the 2008 and 2009 austral winters to a depth of  $\sim 18 \mu\text{K}_{\text{CMB}}$ -arcmin at 150 GHz; 550 deg<sup>2</sup> of it was also mapped to  $\sim 44 \mu\text{K}_{\text{CMB}}$ -arcmin at 95 GHz. Based on optical imaging of all candidates and near-infrared imaging of the majority of candidates, we have found optical and/or infrared counterparts for 158 clusters. Of these, 135 were first identified as clusters in SPT data, including 117 new discoveries reported in this work. This catalog triples the number of confirmed galaxy clusters discovered through the SZ effect. We report photometrically derived (and in some cases spectroscopic) redshifts for confirmed clusters and redshift lower limits for the remaining candidates. The catalog extends to high redshift with a median redshift of  $z = 0.55$  and maximum redshift of  $z = 1.37$ . Forty-five of the clusters have counterparts in the *ROSAT* bright or faint source catalogs from which we estimate X-ray fluxes. Based on simulations, we expect the catalog to be nearly 100% complete above  $M_{500} \approx 5 \times 10^{14} M_{\odot} h_{70}^{-1}$  at  $z \gtrsim 0.6$ . There are 121 candidates detected at signal-to-noise greater than five, at which the catalog purity is measured to be 95%. From this high-purity subsample, we exclude the  $z < 0.3$  clusters and use the remaining 100 candidates to improve cosmological constraints following the method presented by Benson et al. (2011). Adding the cluster data to CMB+BAO+H<sub>0</sub> data leads to a preference for non-zero neutrino masses while only slightly reducing the upper limit on the sum of neutrino masses to  $\sum m_{\nu} < 0.38 \text{ eV}$  (95% CL). For a spatially flat  $\Lambda$ CDM cosmological model, the addition of this catalog to the CMB+BAO+H<sub>0</sub>+SNe results yields  $\sigma_8 = 0.807 \pm 0.027$  and  $w = -1.010 \pm 0.058$ , improving the constraints on these parameters by a factor of 1.4 and 1.3, respectively. The larger cluster catalog presented in this work leads to slight improvements in cosmological constraints from those presented by Benson et al. (2011). These cosmological constraints are currently limited by uncertainty in the cluster mass calibration, not the size or quality of the cluster catalog. A multi-wavelength observation program to improve the cluster mass calibration will make it possible to realize the full potential of the final 2500 deg<sup>2</sup> SPT cluster catalog to constrain cosmology.

*Subject headings:* cosmology – cosmology:cosmic microwave background – cosmology: observations – galaxies: clusters: individual – large-scale structure of universe

cr@bolo.berkeley.edu

<sup>1</sup> Department of Physics, University of California, Berkeley, CA 94720

<sup>2</sup> Harvard-Smithsonian Center for Astrophysics, 60 Garden Street, Cambridge, MA 02138

<sup>3</sup> Kavli Institute for Cosmological Physics, University of Chicago, 5640 South Ellis Avenue, Chicago, IL 60637

<sup>4</sup> Department of Physics, University of Chicago, 5640 South Ellis Avenue, Chicago, IL 60637

<sup>5</sup> Physics Department, Center for Education and Research in Cosmology and Astrophysics, Case Western Reserve University, Cleveland, OH 44106

<sup>6</sup> University of Chicago, 5640 South Ellis Avenue, Chicago, IL 60637

<sup>7</sup> Department of Physics, Ludwig-Maximilians-Universität,

Scheinerstr. 1, 81679 München, Germany

<sup>8</sup> MIT Kavli Institute for Astrophysics and Space Research, Massachusetts Institute of Technology, 77 Massachusetts Avenue, Cambridge, MA 02139

<sup>9</sup> National Center for Supercomputing Applications, University of Illinois, 1205 West Clark Street, Urbana, IL 61801

<sup>10</sup> Department of Physics, Harvard University, 17 Oxford Street, Cambridge, MA 02138

<sup>11</sup> Excellence Cluster Universe, Boltzmannstr. 2, 85748 Garching, Germany

<sup>12</sup> Enrico Fermi Institute, University of Chicago, 5640 South Ellis Avenue, Chicago, IL 60637

<sup>13</sup> Department of Physics, University of Missouri, 5110 Rockhill Road, Kansas City, MO 64110

<sup>14</sup> Department of Astronomy and Astrophysics, University of

## 1. INTRODUCTION

Galaxy clusters are the largest collapsed objects in the Universe, and their abundance is exponentially sensitive to the growth of structure. Measurements of the abundance of galaxy clusters as a function of mass and redshift have the potential to significantly improve current constraints on cosmological parameters, including the equation of state of dark energy and the sum of the neutrino masses (Wang & Steinhardt 1998; Haiman et al. 2001; Holder et al. 2001; Battye & Weller 2003; Molnar et al. 2004; Wang et al. 2004, 2005; Lima & Hu 2007; Shimon et al. 2011). To achieve this objective, a sample of galaxy clusters must have a well understood selection function, good mass estimates, and wide redshift extent.

Most known galaxy clusters have been identified by their optical properties or from their X-ray emission. Clusters of galaxies contain anywhere from tens to thousands of galaxies, but these galaxies account for a small fraction of the total baryonic mass in a cluster (see, e.g. Allen et al. 2011 for a review). Most of the baryons in clusters are contained in the intra-cluster medium (ICM), the hot ( $10^7 - 10^8$  K) X-ray-emitting plasma that pervades cluster environments.

Sunyaev & Zel'dovich (1972) noted that such a plasma would also interact with cosmic microwave background (CMB) photons via inverse Compton scattering, causing a small spectral distortion of the CMB along the line of sight to a cluster. This is called the thermal Sunyaev Zel'dovich (SZ) effect.<sup>1</sup> The amplitude of the spectral

distortion at a given position on the sky is proportional to the integrated electron pressure along the line of sight. Therefore, the integrated thermal SZ (tSZ) flux is a direct measure of the total thermal energy of the ICM, and the SZ flux is thus expected to be a robust proxy for total cluster mass (Barbosa et al. 1996; Holder & Carlstrom 2001; Motl et al. 2005). Additionally, the SZ surface brightness is independent of redshift. As a result, SZ surveys with sufficient angular resolution have the potential to deliver nearly mass-limited cluster samples over a wide redshift range (Carlstrom et al. 2002). Such a cluster sample can provide a growth-based test of dark energy to complement the distance-based tests provided by supernovae (e.g., Riess et al. 1998; Perlmutter et al. 1999); it can also probe the sum of the neutrino masses. Recent results (e.g., Vikhlinin et al. 2009b; Mantz et al. 2010; Benson et al. 2011) have demonstrated the power of such tests to constrain cosmological models and parameters.

However, the SZ signal is faint, exceeding a few hundred  $\mu\text{K}$  for only the most massive (and rare) galaxy clusters. As a result, experiments have only recently achieved the requisite sensitivity to discover previously unknown galaxy clusters. Since the first discovery of clusters using South Pole Telescope (SPT) data (Staniszewski et al. 2009), SZ-selected galaxy cluster catalogs have been produced by the SPT, Atacama Cosmology Telescope (ACT), and *Planck* collaborations (Vanderlinde et al. 2010; Williamson et al. 2011; Marriage et al. 2011; Planck Collaboration et al. 2011). In total, roughly 40 previously unknown clusters discovered via the SZ effect have been published to date.

This is the third SPT cluster catalog and fourth SPT cosmological analysis based on galaxy cluster counts. Vanderlinde et al. (2010, hereafter V10) presented the first SZ-selected catalog, consisting of 21 optically confirmed galaxy clusters found in 2008 SPT data. V10 also investigated the cosmological implications of these clusters, using a simulation-calibrated mass scaling relation. The second SPT cluster catalog and cosmological analysis (Williamson et al. 2011, hereafter W11) used the most massive galaxy clusters discovered in the entire  $2500 \text{ deg}^2$  SPT survey region to test for non-Gaussianity and consistency with  $\Lambda\text{CDM}$ . In the third analysis, Benson et al. (2011, hereafter B11) developed a method to combine X-ray data with the SZ observations, and thereby improve the cluster mass estimates. B11 used this method to improve the cosmological constraints from the V10 cluster sample.

In this work, we present a catalog of 224 SZ-identified galaxy cluster candidates above  $4.5\sigma$  from the first  $720 \text{ deg}^2$  of the SPT survey. Using follow-up optical imaging of all candidates and near-infrared (NIR) imaging for a subset, we estimate redshifts for 158 of the candidates and calculate lower redshift limits for the remaining candidates, which are either too distant to identify with current optical/NIR observations or are spurious detections in the SPT data. The details of the optical and NIR data and redshift estimates are given in a companion paper (J. Song et al. in prep., hereafter S12). Here we summarize the observations and report the resulting redshifts. The clusters with clear optical/NIR counterparts include 117 new discoveries, which increases the

Chicago, 5640 South Ellis Avenue, Chicago, IL 60637

<sup>15</sup> Argonne National Laboratory, 9700 S. Cass Avenue, Argonne, IL, USA 60439

<sup>16</sup> NIST Quantum Devices Group, 325 Broadway Mailcode 817.03, Boulder, CO, USA 80305

<sup>17</sup> Departamento de Astronomia y Astrofisica, PUC Casilla 306, Santiago 22, Chile

<sup>18</sup> Department of Physics, McGill University, 3600 Rue University, Montreal, Quebec H3A 2T8, Canada

<sup>19</sup> Department of Astronomy, University of Florida, Gainesville, FL 32611

<sup>20</sup> Department of Astrophysical and Planetary Sciences and Department of Physics, University of Colorado, Boulder, CO 80309

<sup>21</sup> Department of Space Science, VP62, NASA Marshall Space Flight Center, Huntsville, AL 35812

<sup>22</sup> Department of Physics, University of California, One Shields Avenue, Davis, CA 95616

<sup>23</sup> Physics Division, Lawrence Berkeley National Laboratory, Berkeley, CA 94720

<sup>24</sup> California Institute of Technology, 1200 E. California Blvd., Pasadena, CA 91125

<sup>25</sup> Steward Observatory, University of Arizona, 933 North Cherry Avenue, Tucson, AZ 85721

<sup>26</sup> Department of Physics, University of Michigan, 450 Church Street, Ann Arbor, MI, 48109

<sup>27</sup> Max-Planck-Institut für extraterrestrische Physik, Giessenbachstr. 85748 Garching, Germany

<sup>28</sup> Physics Department, University of Minnesota, 116 Church Street S.E., Minneapolis, MN 55455

<sup>29</sup> Space Telescope Science Institute, 3700 San Martin Dr., Baltimore, MD 21218

<sup>30</sup> Liberal Arts Department, School of the Art Institute of Chicago, 112 S Michigan Ave, Chicago, IL 60603

<sup>31</sup> Department of Physics, Yale University, P.O. Box 208210, New Haven, CT 06520-8120

<sup>32</sup> Berkeley Center for Cosmological Physics, Department of Physics, University of California, and Lawrence Berkeley National Labs, Berkeley, CA 94720

<sup>1</sup> In this work, ‘SZ effect’ will refer to the thermal SZ effect unless specifically noted as the kinetic SZ effect.

number of clusters discovered with the SPT to 144 and triples the total number of SZ-identified clusters. Simulations are used to characterize the SPT cluster selection function. We combine the cluster list with the improved mass-scaling relation from B11 to improve cosmological constraints on large-scale structure, neutrino masses, and the dark energy equation of state.

The paper is organized as follows. We describe the observations and map-making in §2. The extraction of galaxy clusters from the maps is detailed in §3. The optical followup campaign and the resulting redshifts are presented in §4. In §5, we present the complete catalog of galaxy cluster candidates. We review the B11 method for simultaneously constraining cosmological and scaling relation parameters in §6, and we discuss the cosmological constraints from this cluster catalog and prospects for future improvement in §7 before concluding in §8.

## 2. OBSERVATIONS AND DATA REDUCTION

### 2.1. *Telescope and Observations*

The South Pole Telescope (SPT) is a 10-meter telescope designed to survey a large area of the sky at millimeter wavelengths with arcminute angular resolution (Ruhl et al. 2004; Padin et al. 2008; Carlstrom et al. 2011). The first SPT receiver was a three-band (95, 150, and 220 GHz) bolometer camera optimized for studying the primary CMB anisotropy and the tSZ effect. From the time the SPT was commissioned through the end of 2011, the majority of observing time was spent on the recently completed 2500 deg<sup>2</sup> SPT survey. The cluster catalog presented in this paper is derived from the first 720 deg<sup>2</sup> of this survey. This area was observed during the Austral winters of 2008 and 2009. In addition to the early SPT galaxy cluster results discussed in §1, science results from early subsets of the survey data have included measurements of the primary and secondary CMB anisotropy (Keisler et al. 2011; Lueker et al. 2010; Shirokoff et al. 2011; Reichardt et al. 2011), a measurement of gravitational lensing of the CMB (van Engelen et al. 2012), and the discovery of a new population of extremely bright submillimeter galaxies (Vieira et al. 2010).

For cluster-finding, we use data from the SPT 95 GHz and 150 GHz frequency bands. The effective bandcenters for a non-relativistic tSZ spectrum are 97.6 GHz and 152.9 GHz. The 220 GHz band is centered near the tSZ null, so it contains effectively no SZ cluster signal. In the 2008 observing season, the 480 detectors at 150 GHz performed well, but the 95 GHz detectors did not meet specifications. The receiver was reconfigured for the 2009 observing season with 640 detectors at 150 GHz and 160 new detectors at 95 GHz. We observed roughly 170 deg<sup>2</sup> in two fields in 2008 and 550 deg<sup>2</sup> in three fields in 2009. Each field was observed to a minimum depth of 18  $\mu$ K<sub>CMB</sub>-arcmin at 150 GHz.<sup>2</sup> The 2009 fields were observed to a minimum depth of 44  $\mu$ K<sub>CMB</sub>-arcmin at 95 GHz. The SPT map of the first of the two 2008 fields is publicly available (Schaffer et al. 2011).

The standard operating mode of the SPT is to observe a target field by scanning back and forth in azimuth

across the field followed by a step in elevation (Schaffer et al. 2011). One field (RA21HDEC-50) was observed with a hybrid scan strategy including scans at both constant elevation and constant azimuth. This scan strategy changes the filtered point spread function for this field compared to the rest of the data, which affects the SPT signal-to-noise to cluster mass scaling relations presented in §6.2.

The SPT beams have been measured using a combination of bright active galactic nuclei (AGN) in the survey fields and targeted observations of planets (Shirokoff et al. 2011; Keisler et al. 2011). The SPT beam can be described by a main lobe and a diffuse sidelobe. For compact sources such as galaxy clusters, the effect of the sidelobe is degenerate with a calibration factor, and we choose to fold it into the calibration. The SPT main lobe beam is well-described by a Gaussian with FWHM = 1'6 and 1'19 at 95 and 150 GHz respectively. The 2009 data in this work are calibrated using observations of RCW38, a galactic HII region (Staniszewski et al. 2009, W11), while the 2008 data are calibrated by cross-correlating dedicated SPT observations of large patches of sky with WMAP observations of those same regions (V10).

The pointing model is determined using daily observations of galactic HII regions and sensors on the telescope structure sensitive to temperature and mechanical movement (Schaffer et al. 2011). The final pointing in the maps is checked against the positions of radio sources in the Australia Telescope 20 GHz survey (AT20G, Murphy et al. 2010), which has positional accuracy to better than 1 arcsec. The absolute SPT pointing measured in this way is accurate to 3 arcsec. The RMS pointing uncertainty in the maps is 7 arcsec.

### 2.2. *Map Making*

The map-making algorithm for the SPT data has been described in detail in Lueker et al. (2010), Shirokoff et al. (2011), and V10. In overview, the first step is to apply a relative calibration to the time-ordered data (TOD) and then band-pass filter the TOD. Correlated atmospheric signals are removed by subtracting the mean signal across a set of adjacent bolometers. We mask bright point sources detected at  $> 5\sigma$  at 150 GHz ( $> \sim 6$  mJy) before filtering. The pointing for each detector is reconstructed, and the data from each detector are coadded into a map with inverse-noise weighting.

The maps (and cluster list) for the 2008 season are identical to those presented by V10. Maps for the 2009 season have several small differences in the filtering detailed below:

- In V10, the bandpass filter was set by a high-pass filter (HPF) at 0.25 Hz and a low-pass filter at 25 Hz. In 2009, different fields were observed at different scan speeds, so we choose to define the HPF with respect to angular multipole  $\ell$ . The HPF of the 2009 data is at  $\ell = 400$ ; the V10 HPF corresponds to  $\ell \simeq 350$ . As in V10, the HPF is implemented by removing a set of sines and cosines from each scan across the field. We supplement the Fourier mode removal by first fitting and removing a 9<sup>th</sup> order Legendre polynomial from each scan. The higher order (V10 used first order) is necessitated by the large atmospheric modulation intro-

<sup>2</sup> Throughout this work, the unit  $K_{\text{CMB}}$  refers to equivalent fluctuations in the CMB temperature, i.e., the temperature fluctuation of a 2.73 K blackbody that would be required to produce the same power fluctuation.

duced by the subset of observations which scan in elevation. Depending on the observation, this filter acts as a high-pass filter in either the R.A. or decl. direction.

- V10 removed both the mean and slope across the two-dimensional array of all detectors at a single frequency. The 2009 data have four times as many 150 GHz detectors as 95 GHz detectors so the V10 scheme would result in different common mode removal at each frequency. Instead, we follow the treatment in Shirokoff et al. (2011) and remove the mean across sets of neighboring detectors. The 150 GHz detectors are divided into four sets based on their position in the focal plane and the 95 GHz detectors are treated as a single set. This filter set choice produces nearly identical filtering at 95 and 150 GHz.

### 3. CLUSTER EXTRACTION

The procedure used in this work to identify SZ galaxy cluster candidates is identical to that used by W11. We summarize the procedure here and refer the reader to W11 for more details.

Most of the SPT fields have been observed in three frequency bands, centered at 95, 150, and 220 GHz. (Roughly one quarter of the sky area considered in this work was observed in 2008 without 95 GHz coverage.) Each map at a given observing frequency contains contributions from multiple astrophysical signals, and each signal has its own spatial and spectral properties. Because the maps are calibrated in CMB fluctuation temperature units, primary CMB fluctuations and the (small) signal from the kinetic SZ (kSZ) effect contribute equally to all frequencies. Emissive radio galaxies appear in all frequencies with a falling spectral index, while dusty, star-forming galaxies appear with a rising spectral index. Most notably, the 95 GHz and 150 GHz maps contain the tSZ effect signal from galaxy clusters. Because the spectral signature of the tSZ effect is known (up to a small relativistic correction), and because we can roughly predict the spatial profile of the tSZ signal from galaxy clusters, we can combine the maps from the different bands, weighted in spatial frequency space by the expected cluster profile, to maximize the signal-to-noise of the tSZ effect from clusters.

Under certain assumptions about the noise, the astrophysical contaminants, and the source profile, it can be shown (e.g., Melin et al. 2006) that the optimal way to extract a cluster-shaped tSZ signal from our data is to construct a simultaneous spatial-spectral filter, given by

$$\psi(k_x, k_y, \nu_i) = \sigma_\psi^{-2} \sum_j \mathbf{N}_{ij}^{-1}(k_x, k_y) f_{sz}(\nu_j) S_{\text{filt}}(k_x, k_y, \nu_j). \quad (1)$$

Here,  $\sigma_\psi^{-2}$  is the predicted variance in the filtered map

$$\sigma_\psi^{-2} = \sum_{i,j} f_{sz}(\nu_i) S_{\text{filt}}(k_x, k_y, \nu_i) \mathbf{N}_{ij}^{-1}(k_x, k_y) \times \quad (2)$$

$$f_{sz}(\nu_j) S_{\text{filt}}(k_x, k_y, \nu_j),$$

$S_{\text{filt}}$  is the assumed cluster profile convolved with the instrument beam and any filtering performed in the

mapmaking step,  $\mathbf{N}_{ij}$  is the band-band noise covariance matrix (including contributions from astrophysical signals other than cluster tSZ), and  $f_{sz}$  encodes the frequency scaling of the tSZ effect relative to primary CMB fluctuations (e.g., Carlstrom et al. 2002).

As in W11, our model for the astrophysical contribution to  $\mathbf{N}_{ij}$  is a combination of primary and lensed CMB fluctuations, point sources below the SPT detection threshold, kSZ, and tSZ from clusters below the SPT detection threshold. The assumptions about the spatial and spectral shapes of each component are identical to those in W11. As in all previous SPT cluster survey publications, the assumed cluster profile is described by a projected spherical isothermal  $\beta$ -model (Cavaliere & Fusco-Femiano 1976), with  $\beta$  fixed to 1. Twelve different matched filters were constructed and applied to the data, each with a different core radius, spaced evenly between  $0.25'$  and  $3.0'$ . As in previous work, point sources detected above  $5\sigma$  at 150 GHz were masked out to a radius of  $4'$ , with the value inside that radius set to the average of the surrounding pixels from  $4' < r < 4.5'$ . Furthermore, cluster detections within  $8'$  of one of these  $> 5\sigma$  point sources were rejected. Clusters were extracted from the filtered maps with the process used in all previous SPT cluster work and described by V10. As in V10 and W11, we refer to the detection significance maximized across all twelve matched filters as  $\xi$ , and we use  $\xi$  as the primary SZ observable. As in W11, we use only 95 (where available) and 150 GHz data to extract clusters, as adding the 220 GHz data does not result in measurable improvement in cluster yield (see W11 for details).

#### 3.1. Simulations

We use simulations to determine priors on the SZ scaling relations discussed in §6.2 as well as the expected false detection rate for the sample. Simulated sky realizations are filtered to match the real data, and noise realizations based on the measured map noise properties are added.

Each simulated sky is a Gaussian realization of the sum of the best-fit lensed WMAP7  $\Lambda$ CDM primary CMB model, a kSZ model, and point source contributions. The kSZ power spectrum is taken from the Sehgal et al. (2010) simulations and has an amplitude,  $D_l = l(l+1)C_l$ , of  $2.05 \mu\text{K}^2$  at  $\ell = 3000$ . We include both Poisson and clustered point sources. The Poisson contribution reflects both radio source and dusty, star-forming galaxy (DSFG) populations. The amplitude of the radio source term is set by the de Zotti et al. (2005) model source counts to an amplitude  $D_{3000}^r = 1.28 \mu\text{K}^2$  at 150 GHz with an assumed spectral index of  $\alpha_r = -0.6$  (defined by flux  $\propto \nu^\alpha$ ). The amplitude of the Poisson DSFG term at 150 GHz is  $D_{3000}^p = 7.7 \mu\text{K}^2$ . Finally, the clustered DSFG component is modeled by a  $D_\ell \propto \ell$  term normalized to  $D_{3000}^c = 5.9 \mu\text{K}^2$  at 150 GHz. The DSFG terms have an assumed spectral index of 3.6. The amplitude of each component was selected to be consistent with the Shirokoff et al. (2011) bandpowers.

For the determination of the SZ detection significance to cluster mass scaling, we also add a map of the tSZ effect; this tSZ map is not included when estimating the false detection rate. The tSZ map is drawn from a 4000 deg<sup>2</sup> simulation by Shaw et al. (2010). Note that

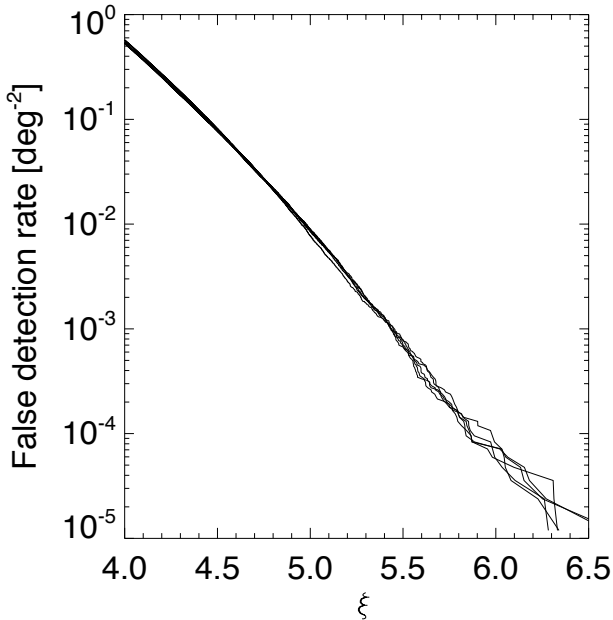


FIG. 1.— Simulated cumulative false detection rates, for each of the five fields, as a function of lower  $S/N$  threshold ( $\xi$ ). No significant differences between the fields are observed. The vertical axis shows the number density of false detections above a given  $S/N$ .

the limited sky area in this simulation means that we reuse the same tSZ maps between different fields in order to get 100 realizations. This limitation does not exist for the Gaussian realizations.

### 3.2. Expected false detection rates

We use the simulations described above, omitting the tSZ component, in order to estimate the rate of false detections arising from noise and non-cluster astrophysical signals. The resulting rates are shown in Fig. 1. As expected, the false detection rate is essentially indistinguishable between the fields; there are the same number of  $N\sigma$  noise fluctuations per unit area. The simulations lead to a prediction of 6.4 false detections in the  $> 5\sigma$  catalog and 59 false detections in the  $> 4.5\sigma$  catalog.

### 3.3. Integrated Comptonization

For each cluster candidate, we estimate the integrated Comptonization by fitting the cluster to a projected spherical  $\beta$ -model with  $\beta = 1$

$$Y(\theta) = y_0 \left(1 + \frac{\theta^2}{\theta_c^2}\right)^{-1}, \quad (3)$$

where  $y_0$  is peak Comptonization and  $\theta_c$  is the angular radius of the cluster core. The integrated Comptonization is defined as

$$Y_{\theta_I} = 2\pi \int_0^{\theta_I} Y(\theta) d\theta. \quad (4)$$

In Table 6, we set  $\theta_I = 1'$  and report  $Y_{1'}$ . We expect measurements of  $Y_{1'}$  to be robust despite the well known degeneracy between  $\theta_c$  and the central Compton parameter  $y_0$  for observations that do not resolve the cluster core (e.g., Planck Collaboration et al. 2011).

The likelihood of a set of cluster model parameters  $\mathcal{H}$  given our set of observed maps  $D_\nu(\bar{x})$  is defined as

$$\log(P(D|\mathcal{H})) = -\frac{1}{2} \sum_{\bar{k}, \nu_1, \nu_2} \frac{(\tilde{D}_{\nu_1}(\bar{k}) - \tilde{s}_{\nu_1}^{\mathcal{H}}(\bar{k}))(\tilde{D}_{\nu_2}(\bar{k}) - \tilde{s}_{\nu_2}^{\mathcal{H}}(\bar{k}))^*}{N_{\nu_1 \nu_2}(\bar{k})}, \quad (5)$$

where  $\tilde{D}_\nu(\bar{k})$  is the Fourier transform of the map for frequency  $\nu$ ,  $\tilde{s}_\nu^{\mathcal{H}}$  is the frequency-dependent Fourier transform of the cluster model for parameters set  $\mathcal{H}$  which we define as  $(\bar{x}, \theta_c, y_0)$ , and  $N_{\nu_1 \nu_2}(\bar{k})$  is the frequency-dependent covariance matrix of the set of maps which accounts for the same noise and astrophysical components used in the matched filter analysis. For the cluster profile, we use the projected spherical  $\beta$ -model defined above. We only fit the profile within  $\theta < 5\theta_c$ .

We use the Rapid Gridded Likelihood Evaluation (RGLE) method (T. Montroy et al., in prep) to evaluate the cluster likelihood and compute  $Y_{1'}$ . The RGL method is based on computing the likelihood for each cluster candidate on a fixed grid in parameter space. In this case, it is a four-dimensional grid over the parameters set  $\mathcal{H}$ . We define the extent of the grid as follows. The 2D position,  $\bar{x}$ , is constrained to be within  $1.5$  of the matched filter position. The central decrement is allowed to range from  $-4.3 \times 10^{-4}$  to  $2.2 \times 10^{-3}$ ; this prior does not impact the results. The core radius,  $\theta_c$ , is required to be between  $0'$  and  $7.5'$ . For cluster candidates at  $z > 0.125$ , we additionally limit the physical core radius ( $r_c$ ) of the cluster to be less than 1 Mpc. We translate between  $r_c$  and  $\theta_c$  based on the redshift of each cluster candidate (or redshift lower limit if unconfirmed). A core radius of 1 Mpc is much larger than the typical cluster size, so this limit allows full exploration of the likelihood degeneracy between  $Y_0$  and  $\theta_c$  while reducing the chance of bias due to noise fluctuations on scales much larger than the expected cluster size.

To compute the probability distribution for  $Y_{1'}$ , we first marginalize the four-dimensional grid over position (i.e.,  $\bar{x}$ ) to determine the two-dimensional likelihood surface for  $(\theta_c, y_0)$ . The value of  $Y_{1'}$  at each  $(\theta_c, y_0)$  is calculated from Eqn. 4 with  $\theta_I = 1'$ . Formally, the likelihood for a given value of  $Y_{1'}$  can be computed by integrating the likelihood surface over curves of constant  $Y_{1'}$ ,

$$P(D|Y_{1'} = Y_i) = \int dY_0 d\theta_c P(D|Y_0, \theta_c) \delta(Y_{1'}(Y_0, \theta_c) - Y_i). \quad (6)$$

The median value and 68% confidence intervals for  $Y_{1'}$  are determined from this likelihood function.

When applying the RGL method to the SPT maps in order to estimate  $Y_{1'}$ , we use the calibration and beam shapes reported in Reichardt et al. (2011). We note that for the 2009 data, these are slightly different from the calibration and beam model described in §2.1 and used in cluster finding in this work. We use maps at 95 GHz (where available) and 150 GHz to estimate the cluster properties. To limit contamination from point sources, we use maps where previously identified point sources have been subtracted. The point source amplitudes are estimated using a variant of the RGL which fits for the point source amplitudes given the beam shape. The point source subtraction significantly changes  $Y_{1'}$  for very

few clusters since all affected point sources are at least  $8'$  away from any cluster candidate.

The RGLE method was previously used in Story et al. (2011) to compute integrated Comptonization for SPT follow-up observations of *Planck* ESZ cluster candidates (Planck Collaboration et al. 2011). The method has been verified by extensive simulations; we have also checked that the RGLE method produces comparable results to an alternative method based on Markov Chain Monte Carlo-based sampling of the likelihood surface (B. Salwanchik et al., in prep).

#### 4. EXTERNAL DATA

In this section, we briefly describe the optical, NIR, and X-ray data associated with this catalog. The optical/NIR followup strategy and analysis methods are summarized here and discussed in detail by S12. We also summarize the dedicated X-ray measurements of 14 SPT clusters, measurements which are used in the cosmological analysis here and which have been discussed in detail in previous SPT publications. Finally, we report X-ray fluxes and luminosities for all candidates that have identified counterparts in the *Roentgensatellit* (*ROSAT*) all-sky survey.

##### 4.1. Optical and NIR Data

Every SPT-selected cluster candidate is followed up with optical imaging observations, and many candidates are also targeted with NIR imaging. Our strategy has evolved over time in order to utilize limited telescope resources to measure redshifts for the majority of cluster candidates. Briefly, the SPT candidates are pre-screened with Digitized Sky Survey (DSS) data. Candidates that appear to be at low redshift are followed up with the 1-meter Swope telescope. Candidates that appear to be at high redshift (i.e., that do not appear in DSS images) are targeted with the 4-m Blanco telescope at CTIO or the 6.5-m Magellan telescopes at Las Campanas Observatory. The 4 – 6 meter class observing is performed using an adaptive strategy, wherein candidates are imaged for a short time in three bands, then with a second pass in two bands if the cluster has not been detected. The second-pass imaging is designed to reach depths sufficient to confirm a  $z \sim 0.9$  cluster. Given weather and other constraints, not all candidates were observed to full depth.

Space-based NIR observations with *Spitzer*/IRAC were obtained at  $3.6 \mu\text{m}$  and  $4.5 \mu\text{m}$  for the subset of candidates above a threshold of  $\xi = 4.8$  ( $\xi \geq 4.5$  for 350  $\text{deg}^2$  of SPT coverage) that were not identified as low redshift clusters in DSS data. Candidates that were not imaged with *Spitzer* — and for which redshifts could not be estimated from the acquired optical data — were targeted with  $K_s$ -band observations with the NEWFIRM camera on the Blanco 4-m.

A number of clusters were also observed using either long-slit or multi-slit spectrographs in subsequent follow-up projects. A robust biweight location estimator (Beers et al. 1990) is used to determine the cluster spectroscopic redshifts from ensemble spectra of member galaxies. Of the clusters in this work, 57 have spectroscopic redshifts, either from the literature or from our targeted observations. The redshifts are shown in Table 6, and the source for every spectroscopic redshift is presented by S12.

##### 4.2. Optical/NIR Imaging Data Reduction and Redshift Determination

All optical images are processed using the PHOTPIPE analysis pipeline (Rest et al. 2005; Miknaitis et al. 2007), as was done in previous SPT optical follow up analyses (High et al. 2010; Williamson et al. 2011; Story et al. 2011). A separate reduction of the optical data from the Blanco Mosaic-II imager is performed using a version of the Dark Energy Survey (DES) data management pipeline (Mohr et al. 2008; Desai et al. 2011), which will eventually be used for analysis of data once the DES begins. The *Spitzer*/IRAC imaging data are processed from the standard online pipeline system and analyzed as described in Ashby et al. (2009); NEWFIRM data are reduced using the FATBOY pipeline (Eikenberry et al. 2006).

Redshifts are estimated for each candidate using three methods as described by S12. The first two methods are based on the identification of red-sequence overdensities and are described in detail in High et al. (2010) and Song et al. (2012b), respectively. The third method estimates photometric redshifts for individual galaxies using the ANNz algorithm (Collister & Lahav 2004), and cluster redshifts are estimated by measuring a peak in a manually-selected red galaxy photometric redshift distribution. For a given cluster candidate, redshift estimates from the three methods are compared, outliers are flagged, and a combined redshift estimate is produced. In cases where only the *Spitzer*/IRAC  $3.6 \mu\text{m}$  and  $4.5 \mu\text{m}$  data are deep enough to detect the cluster, we use the High et al. (2010) method to estimate the redshift. Tests confirm this to be reliable at  $z > 0.7$  and a similar method is described in Stern et al. (2005) and Papovich (2008). These redshifts and associated uncertainties are shown in Table 6. If none of the three methods is successful at estimating a redshift for a given candidate, we report a lower redshift limit based upon the depth of the follow-up imaging.

##### 4.3. X-ray data

###### 4.3.1. Dedicated X-ray Observations of SPT Clusters

As first reported in Andersson et al. (2011, A11), we have obtained *Chandra* and *XMM-Newton* data on 15 of the highest S/N clusters from the 2008 SPT survey fields, including 14 clusters in the redshift range used in the cosmological analysis in this work ( $z > 0.3$ ). B11 updated the X-ray observables for some clusters based on new spectroscopic redshifts (five clusters) or additional *Chandra* observations (five clusters). We refer the reader to A11 and B11 for additional details on these X-ray observations and the analysis of the associated data; the X-ray data here are identical to that used by B11.

From the X-ray data on this 14-cluster sample, density and temperature profiles were derived for use in our cosmological analysis in Section 6. This was done by calculating  $T_X(r)$  and  $M_g(r)$  (allowing the calculation of  $Y_X(r)$  given a reference cosmology) from the X-ray observations of each cluster. Here  $r$  corresponds to a physical radius in the cluster,  $M_g(r)$  is the gas mass,  $T_X$  is the core-excised X-ray temperature, and  $Y_X$  is the product of  $M_g$  and  $T_X$ .

###### 4.3.2. ROSAT Counterparts

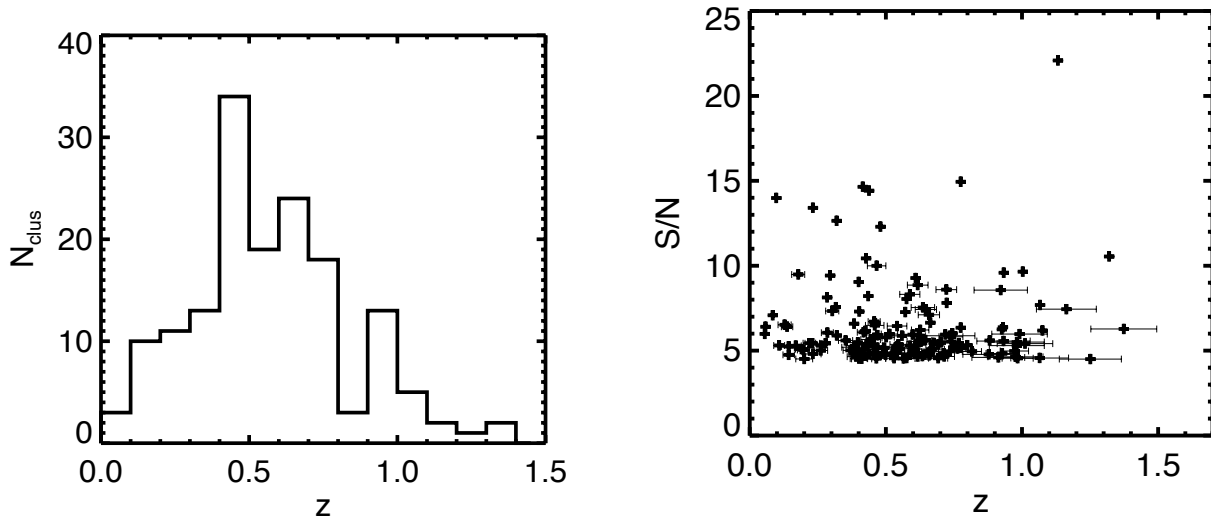


FIG. 2.— *Left panel:* Redshift histogram for the optically confirmed,  $\xi > 4.5$  galaxy clusters in this sample. The median redshift of the sample is 0.55. The median redshift of the sample used in the cosmological analysis ( $z > 0.3$  and  $\xi > 5$ ) is 0.62. *Right panel:* Detection significance versus redshift for all optically confirmed galaxy clusters in this sample.

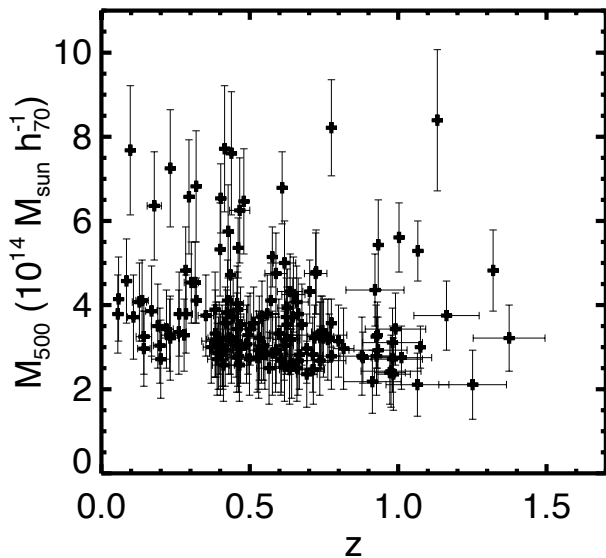


FIG. 3.— Cluster mass estimates versus redshift for all optically confirmed galaxy clusters in this sample. The reported mass has been deboosted and marginalized over the allowed set of cosmological and scaling relation parameters for a  $\Lambda$ CDM cosmology.

A number of cluster candidates are found to be associated with sources in the *ROSAT* Bright or Faint Source Catalog (Voges et al. 1999, 2000). For each of these, Table 1 lists intrinsic X-ray fluxes and rest-frame luminosities in the 0.5–2.0 keV band, inferred from the *ROSAT* count rates. The luminosities assume a reference cosmology chosen to match A11, who assumed a *WMAP7*+*BAO*+ $H_0$   $\Lambda$ CDM preferred cosmology with  $\Omega_M = 0.272$ ,  $\Omega_\Lambda = 0.728$  and  $H_0 = 70.2 \text{ km s}^{-1} \text{ Mpc}^{-1}$  (Komatsu et al. 2011). The absorbing column density of Galactic hydrogen towards each cluster was accounted for using the  $\text{H I}$  survey of Kalberla et al. (2005), and the necessary redshift- and temperature-dependent K-corrections were performed using ICM temperature estimates based on the SPT signal to noise for each cluster

for a simple power-law fit to the A11 data.<sup>3</sup>

These *ROSAT*-derived observables are reported only to provide further confirmation of these clusters; we emphasize that these results are *not* used in the cosmological analysis. Rather, only the X-ray observables from the 14-cluster *Chandra* and *XMM-Newton* dataset from A11 and B11 are used in the cosmological analysis.

## 5. CLUSTER CATALOG

In Table 6, we present the complete list of galaxy cluster candidates from 720  $\text{deg}^2$  of sky surveyed by the SPT. The catalog includes 224 galaxy cluster candidates with detection significance,  $\xi \geq 4.5$ . Using optical/NIR follow-up data (see §4), we have determined redshifts for 158 of the SPT-selected galaxy cluster candidates. The median redshift of the sample is  $z = 0.55$ . The left panel of Figure 2 shows the redshift histogram of our cluster sample. The right panel shows SZ detection significance versus redshift for each cluster with an estimated redshift.

We search for galaxy clusters published in other catalogs within 2 arcmin of every candidate reported in Table 6 and within 5 arcmin of any candidate in Table 6 at  $z \leq 0.3$ . We query the SIMBAD<sup>4</sup> and NED<sup>5</sup> databases, and we manually search more recently published cluster catalogs such as the PLCKESZ (Planck Collaboration et al. 2011) and ACT-CL (Marriage et al. 2011) catalogs. All matches within the appropriate radius are listed in Table 2; whether the associations are physical or random superpositions is discussed in S12.

The optically confirmed, SZ-selected galaxy clusters are found to be massive, with a sharp mass cutoff at approximately  $M_{500} = 2.5 \times 10^{14} M_\odot h_{70}^{-1}$  at  $z = 0.6$ . We define  $M_{500}$  as the mass within a sphere of radius  $r_{500}$ ,

<sup>3</sup> We note, however, that the resulting flux and luminosity estimates are largely insensitive to the temperatures used. For example, adopting the temperature–luminosity relation of Mantz et al. (2010) results in luminosities that differ by  $\sim 2 \pm 2\%$ , far less than the typical statistical uncertainty in the *ROSAT* count rates.

<sup>4</sup> <http://simbad.u-strasbg.fr/simbad>

<sup>5</sup> <http://nedwww.ipac.caltech.edu/>



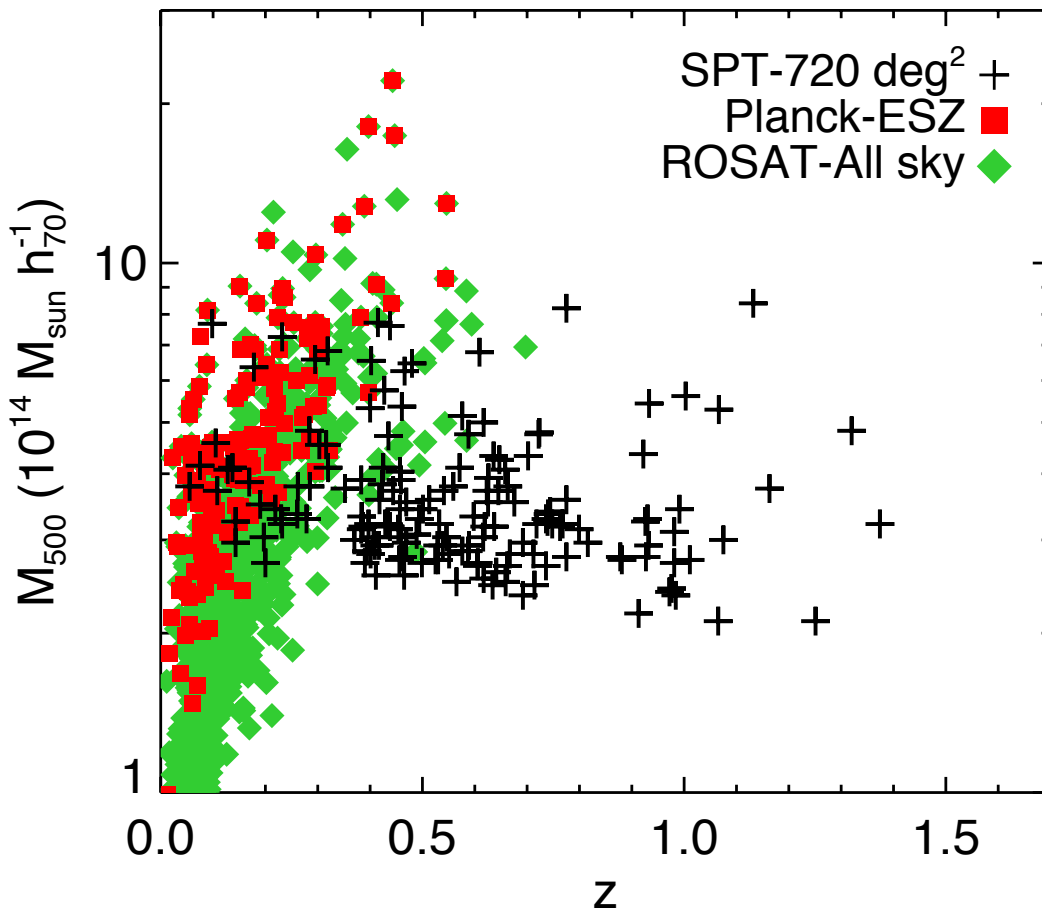


FIG. 4.— Mass estimates versus redshift for three cluster samples: (1) optically-confirmed SZ-selected galaxy clusters from the SPT survey, (2) SZ-selected galaxy clusters from the *Planck* survey (Planck Collaboration et al. 2011), and (3) X-ray selected galaxy clusters from the *ROSAT* all-sky survey (Piffaretti et al. 2011). High resolution SZ surveys, such as that performed with the SPT, uniquely have a nearly redshift independent selection function. The redshift dependent selection in the *Planck* survey is due to beam dilution; the redshift dependence of the *ROSAT* catalog is due to cosmological dimming.

defined as the radius at which the density is 500 times the critical density. The exact mass cutoff depends on the field and cluster redshift. We discuss mass estimates for the clusters in §7.1.2, and we show the estimated masses versus redshift in the left panel of Figure 3. The most massive cluster is SPT-CL J2106-5844 at  $z = 1.1320$  with a mass of  $M_{500} = 8.39 \pm 1.68 \times 10^{14} M_{\odot} h_{70}^{-1}$ . This is the most massive cluster at  $z > 1$  currently known. Foley et al. (2011) showed that although this cluster is rare, it is not in significant tension with the  $\Lambda$ CDM model. The least massive is SPT-CL J2007-4906 at  $z = 1.25 \pm 0.11$  with  $M_{500} = 2.11 \pm 0.82 \times 10^{14} M_{\odot} h_{70}^{-1}$ . The median mass of the sample is  $3.3 \times 10^{14} M_{\odot} h_{70}^{-1}$ .

We compare the mass and redshift distribution of this SPT cluster catalog to cluster catalogs from the *ROSAT* and *Planck* all-sky surveys in Figure 4. For the *ROSAT* all-sky survey, we show 917 clusters taken from the NORAS, REFLEX, and MACS cluster catalogs, as given in the MCXC compilation (Piffaretti et al. 2011). We use the redshift and mass estimates reported by Piffaretti et al. (2011), where the masses were estimated from the

X-ray luminosity-mass relation. We also show the 155 out of 189 galaxy clusters in the *Planck*-ESZ cluster catalog (Planck Collaboration et al. 2011) that have counterparts in the MCXC compilation. The plotted masses and redshifts for these clusters are taken from the MCXC compilation. The mass estimates for the SPT clusters are described in §7.1.2. The selection function of the SPT catalog is nearly independent of redshift. In fact, the minimum mass drops slightly with redshift as the angular size of galaxy clusters decreases, becoming better matched to the SPT beam and less confused by primary CMB fluctuations. This reduction in size with increasing redshift has the opposite effect on the *Planck* SZ survey due to the *Planck* satellite’s larger beam size ( $7'$  at 143 GHz). Beam dilution reduces the *Planck* satellite’s signal-to-noise on high redshift clusters, while the outstanding frequency coverage makes it possible to subtract the primary CMB on large angular scales and recover the SZ signal from low-redshift galaxy clusters. Finally, the *ROSAT* cluster mass threshold rises with redshift due to cosmological dimming of the X-ray flux, crossing over the

TABLE 1  
ROSAT COUNTERPARTS

SPT ID	ROSAT ID	Offset (")	$z$	ROSAT counts ( $s^{-1}$ )	$F_X$ ( $10^{-13}$ ergs $cm^{-2}s^{-1}$ )	$L_X$ ( $10^{44}$ erg $s^{-1}$ )
SPT-CL J0233-5819	1RXS J023303.1-581939	13	0.6630	$0.0295 \pm 0.0131$	2.90	4.63
SPT-CL J0234-5831	1RXS J023443.1-583114	4	0.4150	$0.0800 \pm 0.0200$	7.95	4.12
SPT-CL J0254-5857	1RXS J025427.2-585736	80	0.4380	$0.0846 \pm 0.0305$	7.54	4.41
SPT-CL J0257-5842	1RXS J025744.7-584120	116	$0.43 \pm 0.03$	$0.0725 \pm 0.0298$	6.10	3.66
SPT-CL J0324-6236	1RXS J032412.7-623553	13	$0.72 \pm 0.04$	$0.0260 \pm 0.0121$	2.56	4.85
SPT-CL J0328-5541	1RXS J032833.5-554232	68	0.0844	$0.5700 \pm 0.0300$	47.28	1.31
SPT-CL J0333-5842	1RXS J033317.3-584244	38	$0.47 \pm 0.03$	$0.0125 \pm 0.0056$	1.13	0.82
SPT-CL J0337-6300	1RXS J033754.5-630122	49	$0.45 \pm 0.03$	$0.0166 \pm 0.0079$	1.78	1.22
SPT-CL J0343-5518	1RXS J034259.3-551905	58	$0.51 \pm 0.03$	$0.0167 \pm 0.0071$	1.35	1.21
SPT-CL J0354-5904	1RXS J035420.7-590545	92	$0.46 \pm 0.03$	$0.0105 \pm 0.0049$	0.91	0.62
SPT-CL J0402-6129	1RXS J040245.7-612939	32	$0.52 \pm 0.03$	$0.0082 \pm 0.0039$	0.74	0.70
SPT-CL J0403-5719	1RXS J040352.3-571936	10	$0.46 \pm 0.03$	$0.0391 \pm 0.0081$	3.06	2.11
SPT-CL J0404-6510	1RXS J040421.6-651004	72	$0.14 \pm 0.02$	$0.1300 \pm 0.0200$	13.55	0.74
SPT-CL J0410-6343	1RXS J041009.3-634319	43	$0.50 \pm 0.03$	$0.0291 \pm 0.0103$	2.88	2.44
SPT-CL J0411-6340	1RXS J041129.7-634133	47	$0.14 \pm 0.02$	$0.2600 \pm 0.0300$	25.83	1.26
SPT-CL J0412-5743	1RXS J041206.3-574313	3	$0.39 \pm 0.03$	$0.0231 \pm 0.0074$	1.85	0.88
SPT-CL J0423-5506	1RXS J042315.7-550710	58	$0.20 \pm 0.03$	$0.0332 \pm 0.0125$	2.24	0.25
SPT-CL J0431-6126	1RXS J043126.6-612622	40	0.0577	$0.9800 \pm 0.0700$	82.50	1.14
SPT-CL J0509-5342*	1RXS J050921.2-534159	18	0.4626	$0.0351 \pm 0.0118$	2.79	1.94
SPT-CL J0516-5430	1RXS J051634.0-543104	44	0.2950	$0.1200 \pm 0.0200$	10.86	2.71
SPT-CL J0521-5104	1RXS J052113.2-510419	37	0.6755	$0.0135 \pm 0.0062$	1.20	2.04
SPT-CL J0539-5744	1RXS J054010.1-574354	91	$0.76 \pm 0.03$	$0.0123 \pm 0.0053$	1.47	3.32
SPT-CL J0546-5345*	1RXS J054638.7-534434	69	1.0670	$0.0123 \pm 0.0044$	1.59	7.55
SPT-CL J0551-5709*	1RXS J055126.4-570843	91	0.4230	$0.0271 \pm 0.0053$	3.41	1.96
SPT-CL J0559-5249*	1RXS J055942.1-524950	15	0.6112	$0.0109 \pm 0.0042$	1.29	1.65
SPT-CL J2011-5725	1RXS J201127.9-572507	28	0.2786	$0.1100 \pm 0.0300$	12.25	2.80
SPT-CL J2012-5649	1RXS J201238.3-565038	103	0.0552	$1.1400 \pm 0.0900$	130.40	0.96
SPT-CL J2016-4954	1RXS J201603.5-495530	47	$0.26 \pm 0.03$	$0.0273 \pm 0.0127$	2.98	0.59
SPT-CL J2018-4528	1RXS J201828.7-452720	95	$0.41 \pm 0.03$	$0.0298 \pm 0.0129$	2.97	1.62
SPT-CL J2021-5256	1RXS J202155.7-525721	52	$0.11 \pm 0.02$	$0.0600 \pm 0.0200$	6.62	0.20
SPT-CL J2023-5535	1RXS J202321.2-553534	9	0.2320	$0.0900 \pm 0.0200$	10.58	1.54
SPT-CL J2025-5117	1RXS J202554.4-511647	41	$0.18 \pm 0.02$	$0.0500 \pm 0.0100$	5.12	0.43
SPT-CL J2032-5627	1RXS J203215.2-562753	47	0.2840	$0.0542 \pm 0.0180$	6.64	1.54
SPT-CL J2121-6335	1RXS J212157.9-633459	103	$0.23 \pm 0.03$	$0.1000 \pm 0.0200$	9.85	1.48
SPT-CL J2130-6458	1RXS J213056.1-645909	36	0.3160	$0.0437 \pm 0.0189$	4.33	1.28
SPT-CL J2136-4704	1RXS J213624.5-470453	38	0.4250	$0.0286 \pm 0.0114$	2.58	1.50
SPT-CL J2138-6007	1RXS J213801.2-600801	5	0.3190	$0.0750 \pm 0.0211$	7.74	2.26
SPT-CL J2145-5644	1RXS J214559.3-564455	55	0.4800	$0.0413 \pm 0.0162$	4.01	2.91
SPT-CL J2146-5736	1RXS J214643.9-573723	43	$0.60 \pm 0.03$	$0.0277 \pm 0.0119$	2.64	3.36
SPT-CL J2201-5956	1RXS J220157.8-595648	33	0.0983	$1.0800 \pm 0.0400$	108.10	2.57
SPT-CL J2259-5432	1RXS J225957.0-543118	51	$0.44 \pm 0.04$	$0.0225 \pm 0.0098$	1.68	1.07
SPT-CL J2259-5617	1RXS J230001.2-561709	17	$0.17 \pm 0.02$	$0.1400 \pm 0.0200$	11.29	0.87
SPT-CL J2300-5331	1RXS J230039.8-533118	28	0.2620	$0.0800 \pm 0.0200$	5.81	1.16
SPT-CL J2332-5358*	1RXS J233224.3-535840	17	0.4020	$0.1600 \pm 0.0300$	12.29	6.23
SPT-CL J2337-5942*	1RXS J233726.6-594205	18	0.7750	$0.0271 \pm 0.0136$	2.18	4.64

NOTE. — Cluster candidates coincident with sources in the ROSAT bright or faint source catalogs (Voges et al. 1999, 2000). We define a match if a candidate is within  $5'$  of a cluster candidate at  $z \leq 0.3$  or within  $2'$  of a candidate at  $z > 0.3$ . For each source, we estimate the X-ray luminosity and flux based on the measured redshift, position on the sky, and ROSAT X-ray photon counts. Clusters marked with a "\*" also have  $Y_X$  estimates from XMM or Chandra presented by A11 and B11. Note that SPT-CL J0311-6354 is coincident with 1ES0310-64.0, but not a ROSAT source. We also quote the cluster redshift used in this work (see §4). We include error bars for red sequence redshifts, but not spectroscopic redshifts.

SPT selection function around  $z \sim 0.3$ .

The catalog presented here is expected to be 95% pure for detection significance  $\xi \geq 5$  and 71% pure for detection significance  $\xi \geq 4.5$ . This agrees well with the actual optical and NIR confirmation rate. From §3.2, we expect 59 (6.4) candidates to be false above a detection significance of 4.5 (5). We find 66 (6) candidates do not have optical counterparts, which is in excellent agreement with the expected number of false detections.

### 5.1. Cluster Candidates in the Point-source-masked Regions

As discussed in Section 3, any cluster detections within  $8'$  of an emissive point source detected above  $5\sigma$  at 150 GHz are rejected. We do this because residual source

flux or artifacts due to the masking of these point sources can cause spurious decrements when the maps are filtered. A total area of  $\sim 50$  out of 770 square degrees ( $\sim 6.5\%$ ) was excluded from cluster finding for this reason. This conservative procedure is appropriate for constructing a cluster catalog with a clean, easy-to-define selection function and a mass-observable relation with minimal outliers. However, it is likely that several massive clusters will lie within the exclusion region, and some of those clusters might be only minimally affected by the nearby emissive source. If we assume no spatial correlation between sources and clusters, we would expect roughly eight missed clusters above  $\xi = 5$ .

As in W11, we re-ran the cluster-finding algorithm on

TABLE 2  
CLUSTERS WITH MATCHES IN OTHER CATALOGS

SPT ID	First ID, ref.	All catalogs with match	$z$	Lit. $z$ , ref.
SPT-CL J0254-5857	SPT-CL J0254-5856, A	A,B	0.4380	0.4380, A
SPT-CL J0328-5541	ACO 3126, C	B,C,D,E,F,G	0.0844	0.0844, H
SPT-CL J0404-6510	ACO 3216, C	C	$0.14 \pm 0.02$	0.14, I
SPT-CL J0411-6340	ACO 3230, C	C	$0.14 \pm 0.02$	0.14, I
SPT-CL J0431-6126	Ser 40-6, J	B,C,D,E,F,G,J,K	0.0577	0.0577, H
SPT-CL J0458-5741	ACO 3298, C	C	Unconfirmed	-
SPT-CL J0509-5342	SPT-CL 0509-5342, L	L,M,N	0.4626	0.4626, O
SPT-CL J0511-5154	SCSO J051145-515430, P	M,P	0.6450	0.74, O
SPT-CL J0516-5430	ACO S 0520, C	B,C,G,L,M,N,P	0.2950	0.2950, G
SPT-CL J0521-5104	SCSO J052113-510418, P	M,P	0.6755	0.72, O
SPT-CL J0522-5026	SCSO J052200-502700, P	P	$0.53 \pm 0.04$	0.50, P
SPT-CL J0528-5300	SPT-CL 0528-5300, L	L,M,N,P	0.7648	0.7648, O
SPT-CL J0546-5345	SPT-CL 0547-5345, L	L,M,N	1.0670	1.0670, Q
SPT-CL J0559-5249	SPT-CL J0559-5249, M	M,N	0.6112	0.6112, O
SPT-CL J2011-5725	RXC J2011.3-5725, G	G	0.2786	0.2786, G
SPT-CL J2012-5649	Str 2008-569, K	B,C,E,G,K,R	0.0552	0.0552, H
SPT-CL J2020-4646	ACO 3673, C	C	$0.19 \pm 0.02$	-
SPT-CL J2021-5256	Ser 138-5, J	C,G,J	$0.11 \pm 0.02$	-
SPT-CL J2023-5535	RXC J2023.4-5535, G	A,B,G	0.2320	0.2320, G
SPT-CL J2025-5117	ACO S 0871, C	C	$0.18 \pm 0.02$	-
SPT-CL J2032-5627	CIG 2028.3-5637, S	C,G,S	0.2840	0.0608, H
SPT-CL J2055-5456	ACO 3718, C	C,G	$0.13 \pm 0.02$	-
SPT-CL J2059-5018	ACO S 0912, C	C	$0.41 \pm 0.03$	-
SPT-CL J2101-5542	ACO 3732, C	C	$0.20 \pm 0.02$	-
SPT-CL J2121-6335	ACO S 0937, C	C	$0.23 \pm 0.03$	-
SPT-CL J2201-5956	CIG 2158.3-6011, S	A,B,C,D,E,F,G,S	0.0972	0.0972, H
SPT-CL J2259-5617	ACO 3950, C	C,M	$0.17 \pm 0.02$	-
SPT-CL J2300-5331	ACO S 1079, C	C,M	0.2620	0.29, O
SPT-CL J2332-5358	SCSO J233227-535827, P	M,P	0.4020	0.32, T
SPT-CL J2351-5452	SCSO J235138-545253, P	P	0.3838	0.3838, U

NOTE. — Cluster candidates coincident with galaxy clusters identified in other catalogs. We define a match if a candidate is within  $5'$  ( $2'$ ) of an identified cluster for clusters at  $z < 0.3$  ( $z > 0.3$  or unconfirmed). For each match, we report the name under which the cluster was first reported and all catalogs which include the cluster. See S12 for a discussion of physical association vs. random superposition for these matches. We also quote the cluster redshift used in this work—either the photometric redshift estimated in S12 or a spectroscopic redshift obtained from followup observations or the literature. We include error bars for red sequence redshifts but not spectroscopic redshifts. In the last column, we quote a redshift from the literature if available. Error bars are not reported for literature redshifts; two (four) significant digits are used if the literature redshift is photometric (spectroscopic).

A SPT-CL catalog. W11

B PLCKESZ catalog. Planck Collaboration et al. (2011)

C ACO catalog. Abell et al. (1989)

D APMCC catalog. Dalton et al. (1997)

E [DBG99] catalog. de Grandi et al. (1999)

F [DEM94] catalog. Dalton et al. (1994)

G REFLEX catalog. Böhringer et al. (2004)

H Struble & Rood (1999)

I Ebeling et al. (1996)

J Sersic catalog. Sérsic (1974)

K Stromlo catalog. Duus & Newell (1977)

L SPT-CL catalog. Staniszewski et al. (2009)

M SPT-CL catalog. V10

N ACT-CL catalog. Marriage et al. (2011)

O H10

P SCSO catalog. Menanteau et al. (2010)

Q Brodwin et al. (2010)

R [QW] catalog. Quintana & White (1990)

S CIG catalog. Feitsova (1981)

T Šuhada et al. (2010)

U Buckley-Geer et al. (2011)

TABLE 3  
CLUSTER CANDIDATES ABOVE  $\xi = 5$  IN THE  
SOURCE-MASKED AREA

SPT ID	RA	DEC	$\xi$	$\theta_c$
SPT-CL J0334-6008	53.7116	-60.1541	6.97	1.25
SPT-CL J0434-5727	68.6517	-57.4568	5.07	0.75
SPT-CL J0442-5905	70.6707	-59.0975	6.42	0.25
SPT-CL J2142-6419	325.7280	-64.3268	11.01	0.25
SPT-CL J2154-5952	328.7210	-59.8878	7.16	0.50
SPT-CL J2154-5936	328.7230	-59.6121	6.28	0.50

NOTE. — Cluster candidates identified in a non-standard cluster-finding analysis, in which only the very brightest ( $> 100$  mJy) point sources are masked (see text for details). Only candidates from the area masked in the standard analysis are listed here. These candidates are not included in the cosmological analysis or in the total number of candidates quoted in the text.

all the fields used in this work with only the very brightest sources masked. For this work we used a brightness threshold of  $S_{150\text{GHz}} > 100$  mJy, compared to the normal threshold of  $\sim 6$  mJy, resulting in a total masked area of  $< 3$  square degrees. Each detection with  $\xi \geq 5$  from the originally masked area was visually inspected (below the  $\xi = 5$  threshold, it becomes too difficult to distinguish visually between real clusters and artifacts), and the vast majority were rejected as obvious point-source-related artifacts. Some detections, however, did appear to be significant SZ decrements only minimally affected by the nearby source. These objects are listed in Table 3. We find six objects above  $\xi = 5$ , consistent within Poisson uncertainties with the expected number. One of these objects, SPT-CL J2142-6419, was also identified in the auxiliary detection procedure in W11. Two of the six objects (SPT-CL J2154-5952 and SPT-CL J2154-5936) are unusually close to one another on the sky ( $16'5$  separation), but visual inspection shows nothing out of the ordinary about either candidate beyond its proximity to an emissive source.

We have not yet attempted to obtain redshifts for these six cluster candidates, and they are not included in the cosmological analysis or in the total number of candidates quoted in the rest of the text. We perform the same search for counterparts to these six candidates in other galaxy cluster catalogs as we do for the main sample. We find no galaxy cluster matches, though we do find X-ray sources within 5 arcmin of SPT-CL J0334-6008 and within 2 arcmin of SPT-CL J0434-5727, SPT-CL J0442-5905, and SPT-CL J2154-5936.

## 6. COSMOLOGICAL MODELING

In this section, we briefly review the method presented by B11 to use the combination of an SZ-selected cluster catalog and X-ray follow-up observations to investigate cosmological constraints; we refer the reader to B11 for a complete description. We also present a slightly modified algorithm to treat fields of varying depths.

We use Monte Carlo Markov chain (MCMC) methods to determine parameter constraints. As outlined by B11, we have extended CosmoMC<sup>6</sup> (Lewis & Bridle 2002) to simultaneously fit the SZ and X-ray cluster observable-

mass relations while also varying cosmological parameters. We include all  $\xi > 5$  and  $z > 0.3$  cluster candidates in this catalog (100 clusters) in the cosmological analysis as well as the X-ray observations of 14 SPT-selected clusters described by A11 and B11. These data will be referred to as SPT<sub>CL</sub>.

In addition to the cluster data, some MCMCs include CMB data from WMAP7 and SPT (Komatsu et al. 2011; Keisler et al. 2011). In some cases, we also add measurements of the BAO feature using SDSS and 2dFGRS data (Percival et al. 2010), low-redshift measurements of  $H_0$  from the Hubble Space Telescope (Riess et al. 2011), or measurements of the luminosity-distance relationship from the Union2 compilation of 557 SNe (Amanullah et al. 2010). Finally, we sometimes use a BBN prior on the baryon density from measurements of the abundances of deuterium (Kirkman et al. 2003). In all cases, we set the helium abundance based on the predictions of BBN (Hamann et al. 2008).

### 6.1. X-ray scaling relations

Following Vikhlinin et al. (2009b) and B11, we use  $Y_X$  as an X-ray proxy for cluster mass,  $M_{500}$ . We assume a  $Y_X - M_{500}$  relation of the form

$$\frac{M_{500}}{10^{14}M_{\odot}/h} = \left(A_X h^{3/2}\right) \left(\frac{Y_X}{3 \times 10^{14}M_{\odot} \text{keV}}\right)^{B_X} \left(\frac{H(z)}{H_0}\right)^{C_X}, \quad (7)$$

parameterized by the normalization  $A_X$ , the slope  $B_X$ , the redshift evolution  $C_X$ , and a log-normal scatter  $D_X$  on  $Y_X$ . We express the mass in units of  $M_{\odot}/h$  to match the  $\zeta - M_{500}$  relation in Section 6.2. For our cosmological analysis, we assume the same Gaussian priors on the scaling relation parameters as B11. The priors are motivated by constraints from X-ray measurements by Vikhlinin et al. (2009a) and simulations. The Gaussian priors are  $A_X = 5.77 \pm 0.56$ ,  $B_X = 0.57 \pm 0.03$ ,  $C_X = -0.4 \pm 0.2$ , and  $D_X = 0.12 \pm 0.08$ . For the cosmological results in this paper, only the uncertainty on  $A_X$  matters; we have tested fixing the other parameters to their central values and find essentially identical results.

### 6.2. SZ scaling relations

As in V10 and B11, we estimate galaxy cluster masses according to an SZ signal-to-noise to mass scaling relation. Following those works, we introduce the unbiased significance,  $\zeta$ , since the relation between  $\xi$  and halo mass is complicated by the comparable effects of intrinsic scatter and instrumental noise. The unbiased significance is defined to be the average detection signal-to-noise of a simulated cluster, measured across many noise realizations, and related to the detection significance  $\xi$  as follows:

$$\zeta = \sqrt{\langle \xi \rangle^2 - 3} \quad (8)$$

at  $\xi > 2$ . The detection significance  $\xi$  is maximized across possible cluster positions and filters scales, effectively adding three degrees of freedom to the fit. The unbiased significance  $\zeta$  removes this maximization bias.

The specific form of the scaling relation is:

$$\zeta = A_{SZ} \left(\frac{M_{500}}{3 \times 10^{14}M_{\odot}h^{-1}}\right)^{B_{SZ}} \left(\frac{H(z)}{H(0.6)}\right)^{C_{SZ}}, \quad (9)$$

<sup>6</sup> <http://cosmologist.info/cosmomc/>

TABLE 4  
SZ-MASS NORMALIZATION PER FIELD

Name	Year	Scaling factor
RA5H30DEC-55	2008	1.00
RA23H30DEC-55	2008	1.01
RA3H30DEC-60	2009	1.25
RA21HDEC-50	2009	1.09
RA21HDEC-60	2009	1.31

NOTE. — The estimated scaling factors for the mass normalization  $A_{SZ}$  for each field. These factors correct for the different noise levels in each field.

where  $A_{SZ}$  is a normalization,  $B_{SZ}$  a mass evolution, and  $C_{SZ}$  a redshift evolution. The method to go from simulations to an SZ signal-to-noise to mass scaling relation is described in more detail by V10.

As described more fully in V10, this scaling relation is based on SZ simulations of approximately  $4000 \text{ deg}^2$  of sky. The simulations used in this work are described in §3.1. The intrinsic scatter,  $D_{SZ}$ , was measured to be 24%. The main uncertainty for cosmological purposes is on the mass normalization,  $A_{SZ}$ , which is assumed to be uncertain at the 30% level.

Unlike V10, this analysis includes fields with substantially different noise levels. We have repeated the simulations (see §3.1) on each field, and find the main effect is an overall rescaling of the expected SZ signal-to-noise for a given cluster mass, i.e., a change to  $A_{SZ}$ . There is a slight change to the redshift evolution between fields as well, but neglecting this results in an additional percent level scatter which is completely negligible given the overall 24% scatter in the scaling relation. We have also checked the simulations by adding known cluster profiles to the real maps, applying the cluster-finding algorithm and checking the recovered signal-to-noise. This semi-analytic test agrees well with the results of the simulations. We apply a fixed rescaling of  $A_{SZ}$  to each field, as tabulated in Table 4. The normalization of the rescaling is chosen such that the RA5H30DEC-55 field is unity. We use simulations of all five fields to estimate the parameters  $A_{SZ}$ ,  $B_{SZ}$ ,  $C_{SZ}$ , and  $D_{SZ}$  for the combined scaling relation, and determine values of 6.24, 1.33, 0.83, and 0.24 respectively. Uncertainties in the SZ modeling lead to significant systematic uncertainties on these scaling relation parameters. Following V10, we apply conservative 30%, 20%, 50%, and 20% Gaussian uncertainties to  $A_{SZ}$ ,  $B_{SZ}$ ,  $C_{SZ}$ , and  $D_{SZ}$ , respectively.

### 6.3. Cluster likelihood function

We have written a module extension to CosmoMC to calculate the cluster likelihood function. In essence, this module uses the Cash statistic (Cash 1979) to compare the observed number counts to a known Poisson distribution at each step in the MCMC. The method closely mirrors that presented by B11, to whom we refer the reader for a complete description. Briefly, we use the Tinker mass function (Tinker et al. 2008) to calculate the mass function based on the cosmological parameters and associated matter power spectra estimated by CAMB (Lewis et al. 2000) at 20 logarithmically spaced redshifts between  $0 < z < 2.5$ . The mass function is calculated for an

over-density of 500 times the critical density. Using the scaling relation parameters at that step of the MCMC, the mass function is translated from the native  $M_{500-z}$  space into the three-dimensional observable space, with axes corresponding to the SZ detection significance  $\xi$ , the X-ray parameter  $Y_X$ , and the optically derived redshift  $z$ . The observed number counts are compared to the expectation values in this three dimensional space to evaluate the likelihood for that step of the MCMC.

There are two differences between the likelihood function used in this work and that presented by B11. The most significant of these is the field-dependent SZ scaling relation described in §6.2. In practice, this means that the above calculation is done separately for each of the five fields, and the resulting log likelihoods are summed.

The treatment of unconfirmed cluster candidates is the second, more minor difference between this work and B11. B11 left unconfirmed clusters out of the analysis; this is appropriate given the extremely high redshift lower limit on the single unconfirmed (and almost certainly false) cluster candidate in that cluster sample. A more rigorous treatment includes the likelihood of each unconfirmed candidate, using the expectation value of the candidate being either a higher redshift cluster or a false detection. This expectation value is the sum of the expected number of false detections at a given detection significance and a redshift-dependent selection function convolved by the mass function. In practice, the treatment of unconfirmed clusters is nearly negligible since the  $S/N > 5$  sample used to derive cosmological constraints has high purity and the precision of the cosmological constraints is currently limited by the systematic mass calibration uncertainty.

With this in mind, we make two simplifying approximations in our implementation. First, we neglect any cosmological dependence in the false detection rate – the simulations used to calculate the false detection rate are only run for one cosmological model. This effect should be negligible since the CMB and foreground power levels are well-known. Second, we treat the redshift selection function as a Heaviside function at the quoted redshift limit for that cluster. The chance of detecting a cluster out to this redshift is nearly unity with the current optical and NIR observations. We have tested shifting the Heaviside function to  $z > 1.5$  or  $z > 2$  and find no impact on the cosmological constraints. This can be understood intuitively because (a) the overall purity is high, and (b) the expected number of unconfirmed, real, high-redshift clusters is small compared to the expected number of false detections.

## 7. COSMOLOGICAL IMPLICATIONS

We present cosmological constraints from the SPT cluster sample in this section. The main results are tabulated in Table 5. We first consider the baseline, six-parameter  $\Lambda$ CDM model, and highlight the improvement in parameter constraints for the current catalog compared to the smaller B11 catalog. The uncertainty in the cosmological analysis is dominated by the systematic cluster mass uncertainty; the mass calibration is based on the same X-ray data and  $Y_X - M$  scaling relation used in the analysis of B11. The  $Y_X - M$  scaling relation was observationally measured using X-ray measurements of the total mass derived assuming hydro-

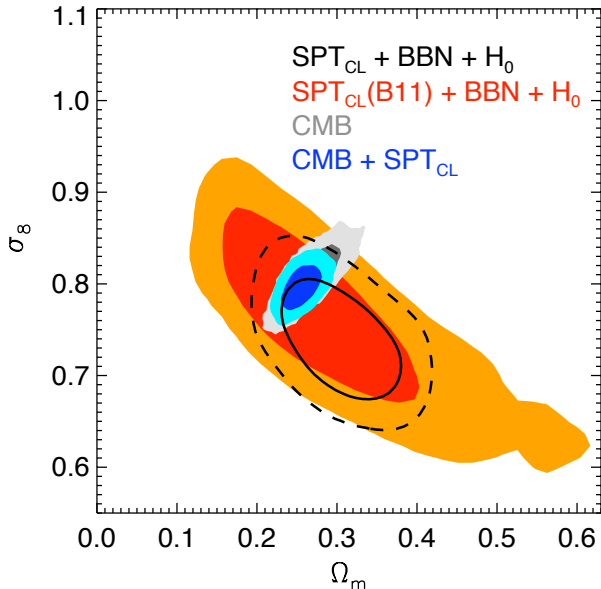


FIG. 5.— 68% and 95% likelihood contours in the  $\Omega_m - \sigma_8$  plane for different datasets. The additional clusters in this catalog reduce the allowed parameter volume by a factor of two compared to B11 when considering the  $\text{SPT}_{\text{CL}} + \text{BBN} + H_0$  data. However, the linear combination showing the most improvement is already well constrained by the CMB data. Therefore as predicted by B11, the additional clusters will not substantially improve constraints for the  $\text{CMB} + \text{SPT}_{\text{CL}}$  data until the mass calibration is improved.

static equilibrium, with the absolute calibration cross-checked by weak-lensing-based mass estimates. We also compare the observed and expected cluster abundances, and we estimate the masses of each galaxy cluster. We next examine cosmological constraints for two extensions beyond a  $\Lambda$ CDM model, testing the ability of the cluster sample to constrain the dark energy equation of state and the sum of the neutrino masses. These two model extensions are degenerate in the current cluster data; we choose to look at independent constraints on each while fixing the other parameter to the  $\Lambda$ CDM baseline value. Finally, we discuss prospects for improving the mass calibration and thereby realizing the full potential of SZ-selected galaxy clusters as cosmological probes.

### 7.1. $\Lambda$ CDM constraints

In a  $\Lambda$ CDM model, cluster samples primarily constrain  $\sigma_8$  and  $\Omega_m$  (see e.g., B11, Rozo et al. 2010). As was done by B11, we look at “cluster-only” constraints based on  $\text{SPT}_{\text{CL}} + \text{BBN} + H_0$  with the reionization optical depth fixed to  $\tau = 0.08$ . The external data and  $\tau$  prior are required since cluster abundances are insensitive to several  $\Lambda$ CDM parameters, including  $\tau$ . We see a substantial improvement in the  $\text{SPT}_{\text{CL}} + \text{BBN} + H_0$  constraints with the expanded cluster catalog from this work; the allowed likelihood volume is reduced by approximately a factor of two (compare the filled red/orange contours and black contours in Fig. 5).

Adding the new SPT cluster sample to the WMAP7 and SPT CMB power spectrum data improves the constraints on  $\Omega_m, \Omega_c h^2, \sigma_8,$  and  $h$  by roughly a factor of 1.5 over the CMB alone. The constraints are listed in the first two columns of Table 5. The cluster data modestly tightens constraints on the amplitude of the primordial

power spectrum as well. The uncertainty on the amplitude is reduced by 24% from  $\ln(10^{10} A_s) = 3.196 \pm 0.042$  to  $3.176 \pm 0.034$ .

However, these constraints are only marginally better than those presented by B11. As shown in Fig. 5, the  $\text{SPT}_{\text{CL}}$  constraints in the  $\Omega_m - \sigma_8$  plane are most improved along a direction well-constrained by the CMB data. For constraints in the perpendicular direction, the  $\text{SPT}_{\text{CL}}$  data are limited by the current mass calibration uncertainty, determined from the  $Y_X - M$  scaling relation which is unchanged from B11. A better mass calibration will be essential to realize the full potential of cosmological constraints from galaxy clusters.

#### 7.1.1. Comparison to expected number counts

We can compare the observed number of galaxy clusters with the number expected for a given cosmological model. We compare the high-purity sample of 100 cluster candidates at  $z > 0.3$  and  $\xi > 5$  to the expected number counts for two cases with a  $\Lambda$ CDM cosmology. The first case uses only non-cluster data ( $\text{CMB} + \text{BAO} + \text{SN} + H_0$ ) with the scaling relations allowed to vary across the conservatively wide simulation-based prior. The symmetric  $1\sigma$  range around the median is [121, 805] candidates and the  $2\sigma$  range is [37, 2004] candidates. The likelihood peaks near 130 candidates. In the second case, we add the cluster catalog data while allowing the scaling relations to vary. As would be expected, this MCMC leads to a tighter predicted range of candidate counts with roughly Poisson scatter around the observed number counts. The  $1\sigma$  range is [92, 111] candidates with the median at 101 objects. The difference between the two cases is primarily due to the range of scaling relation parameters explored. We do not see significant tension with the observed cluster counts in either case.

#### 7.1.2. Mass estimates

We present mass estimates based on the posterior probability distributions for all optically confirmed clusters in Table 6. In all cases, we quote  $M_{500}$ , as defined in §5. For the 15 clusters with X-ray data from A11, these are joint X-ray and SZ mass estimates. Only the SZ data are used for the other clusters. We calculate a probability density function on a mass grid at each point in the  $\text{CMB} + \text{BAO} + \text{SN} + H_0 + \text{SPT}_{\text{CL}}$  parameter chain for a  $\Lambda$ CDM cosmology. The allowed  $\Lambda$ CDM parameter ranges for this data set are essentially unchanged from the  $\text{CMB} + \text{SPT}_{\text{CL}}$  data set. These probability density functions are combined to obtain a mass estimate that has been fully marginalized over all cosmological and scaling relation parameters.

### 7.2. Dark energy equation of state

We next examine cosmological constraints in a wCDM cosmology. This model introduces the dark energy equation of state,  $w$ , as a free parameter (in the  $\Lambda$ CDM model,  $w$  is fixed to  $-1$ ). The equation of state remains constant with time. The cluster abundance and the shape of the mass function depend on  $w$  through its effect on the expansion history of the Universe and the growth of structure.

The best external constraints on  $w$  come from a combination of the CMB, BAO,  $H_0$ , and SNe data. Adding

TABLE 5  
COSMOLOGICAL CONSTRAINTS

	$\Lambda$ CDM		wCDM		$\sum m_\nu$	
	CMB	+SPT <sub>CL</sub>	CMB + BAO + H <sub>0</sub> + SNe	+ SPT <sub>CL</sub>	CMB + BAO + H <sub>0</sub>	+ SPT <sub>CL</sub>
$\Omega_c h^2$	$0.1109 \pm 0.0048$	$0.1086 \pm 0.0031$	$0.1140 \pm 0.0041$	$0.1104 \pm 0.0029$	$0.1113 \pm 0.0030$	$0.1113 \pm 0.0025$
$\sigma_8$	$0.808 \pm 0.024$	$0.798 \pm 0.017$	$0.840 \pm 0.038$	$0.807 \pm 0.027$	$0.775 \pm 0.041$	$0.766 \pm 0.028$
$\Omega_m$	$0.267 \pm 0.026$	$0.255 \pm 0.016$	$0.269 \pm 0.014$	$0.262 \pm 0.013$	$0.274 \pm 0.016$	$0.275 \pm 0.015$
$H_0$	$70.71 \pm 2.17$	$71.62 \pm 1.53$	$71.20 \pm 1.49$	$71.15 \pm 1.51$	$69.83 \pm 1.36$	$69.76 \pm 1.31$
$w$			$-1.054 \pm 0.073$	$-1.010 \pm 0.058$		
$\sum m_\nu$ (95% CL)					$< 0.44$	$< 0.38$

NOTE. — Cosmological constraints for three models with and without the SPT cluster sample.

the SPT cluster sample to this data set reduces the uncertainty on the dark energy equation of state by a factor of 1.3 to give  $-1.010 \pm 0.058$ . This value is completely consistent with a cosmological constant and within  $1\sigma$  of the no-cluster constraint of  $w = -1.054 \pm 0.073$ . These results are shown in Figure 6 and tabulated in Table 5.

The cluster data also aid in the measurement of the dark matter density and  $\sigma_8$ . The addition of clusters moves the preferred cold dark matter density down by nearly  $1\sigma$  from  $\Omega_c h^2 = 0.1140 \pm 0.0041$  to  $\Omega_c h^2 = 0.1104 \pm 0.0029$ . As would be expected, the amplitude of the matter power spectrum also drops from  $\sigma_8 = 0.840 \pm 0.038$  to  $0.807 \pm 0.027$ . The uncertainties on both parameters are reduced by a factor of 1.4 with the addition of the SPT cluster data.

We can compare the wCDM results to those reported by B11 based on fewer clusters but the same X-ray data and mass calibration uncertainty. B11 report  $\sigma_8 = 0.793 \pm 0.028$  and  $w = -0.973 \pm 0.063$  for the CMB + BAO + SNe + SPT<sub>CL</sub>(B11) data. In this analysis, the median  $\sigma_8$  and  $w$  values shift by  $\sim 0.5\sigma$  relative those presented by B11, and the uncertainties tighten slightly. These changes are primarily due to including the local measurement of  $H_0$  in the constraints, rather than the additional clusters. We also ran chains without  $H_0$  to parallel the B11 treatment and both differences effectively disappear.

### 7.3. Massive neutrinos

The second extension to a  $\Lambda$ CDM model that we consider is a non-zero sum of neutrino masses,  $\sum m_\nu \geq 0$ . Non-zero neutrino masses are well-motivated by the measured mass differences in neutrino oscillation experiments (e.g., Ahmad et al. 2002; Eguchi et al. 2003; Ashie et al. 2004). For CMB + H<sub>0</sub> + BAO, neutrino masses are highly degenerate with  $\sigma_8$ , as shown in Figure 7. Cluster abundances are an independent measure of local structure ( $\sigma_8$ ), and thereby enable better constraints on the sum of the neutrino masses. In this work, we assume a thermal background of three degenerate mass neutrino species.

The main results with massive neutrinos are shown in Figure 7 and tabulated in Table 5. Adding the SPT cluster sample to the CMB + H<sub>0</sub> + BAO data leads to a small preference for a positive neutrino mass sum. If we fit the 1-D posterior on the total neutrino mass with a Gaussian (avoiding the bias to the median and 68%

interval values due to the positivity prior), the preferred value is  $\sum m_\nu = 0.17 \pm 0.13$  eV. The uncertainties on the neutrino mass tighten with the addition of the cluster data, but the shift in the peak likelihood towards higher masses means that the 95% confidence upper limit on  $\sum m_\nu$  is nearly unchanged:  $\sum m_\nu < 0.44$  eV without clusters and  $\sum m_\nu < 0.38$  eV with clusters. This improvement is largely due to the tighter constraint on  $\sigma_8$  derived from the cluster data. The SPT<sub>CL</sub> data tightens the  $\sigma_8$  measurement from the CMB + BAO + H<sub>0</sub> data from  $0.775 \pm 0.041$  to  $0.766 \pm 0.028$ .

We again compare these results to those reported by B11. B11 report  $\sigma_8 = 0.770 \pm 0.026$  and a 95% CL upper limit of  $\sum m_\nu < 0.33$  eV for the CMB + H<sub>0</sub> + BAO + SPT<sub>CL</sub>(B11) data. The median  $\sigma_8$  value has shifted down slightly in this work leading to a higher  $\sum m_\nu$  limit. The parameter uncertainties are essentially unchanged.

### 7.4. Prospects for Further Improvement

The cosmological results in this paper are derived from a high-purity and high-redshift subsample of the catalog consisting of 100 galaxy clusters. The full SPT survey covers approximately 3.5 times the sky area used in this work and is being used to produce a similar high purity catalog with 3.5 times as many clusters. Realizing the scientific potential of this sample will require significant improvements to the current mass calibration. We have simulated the impact of a more accurate mass calibration on both the current catalog and the full SPT survey. A 5% mass calibration would tighten the current constraints to  $\sigma(w) = 0.043$  (for CMB + BAO + H<sub>0</sub> + SNe + SPT<sub>CL</sub>) and  $\sigma(\sum m_\nu) = 0.10$  eV (for CMB + BAO + H<sub>0</sub>) respectively, a factor of 1.3 better than those listed in Table 5 for the current mass calibration. Determining the mass calibration to better than 5% would have little impact with the current catalog. However, it would significantly improve constraints for the  $\times 3.5$  larger, full SPT sample and could make possible a significant detection of the sum of the neutrino masses.

As laid out by B11, four approved observation programs are being pursued by the SPT collaboration to independently test the cluster mass calibration, with the goal of reducing this uncertainty to a level  $\lesssim 5\%$ . First, X-ray observations with *Chandra* are scheduled for the 80 most-significant SPT cluster detections at  $z > 0.4$ . Second, we have been awarded time for weak

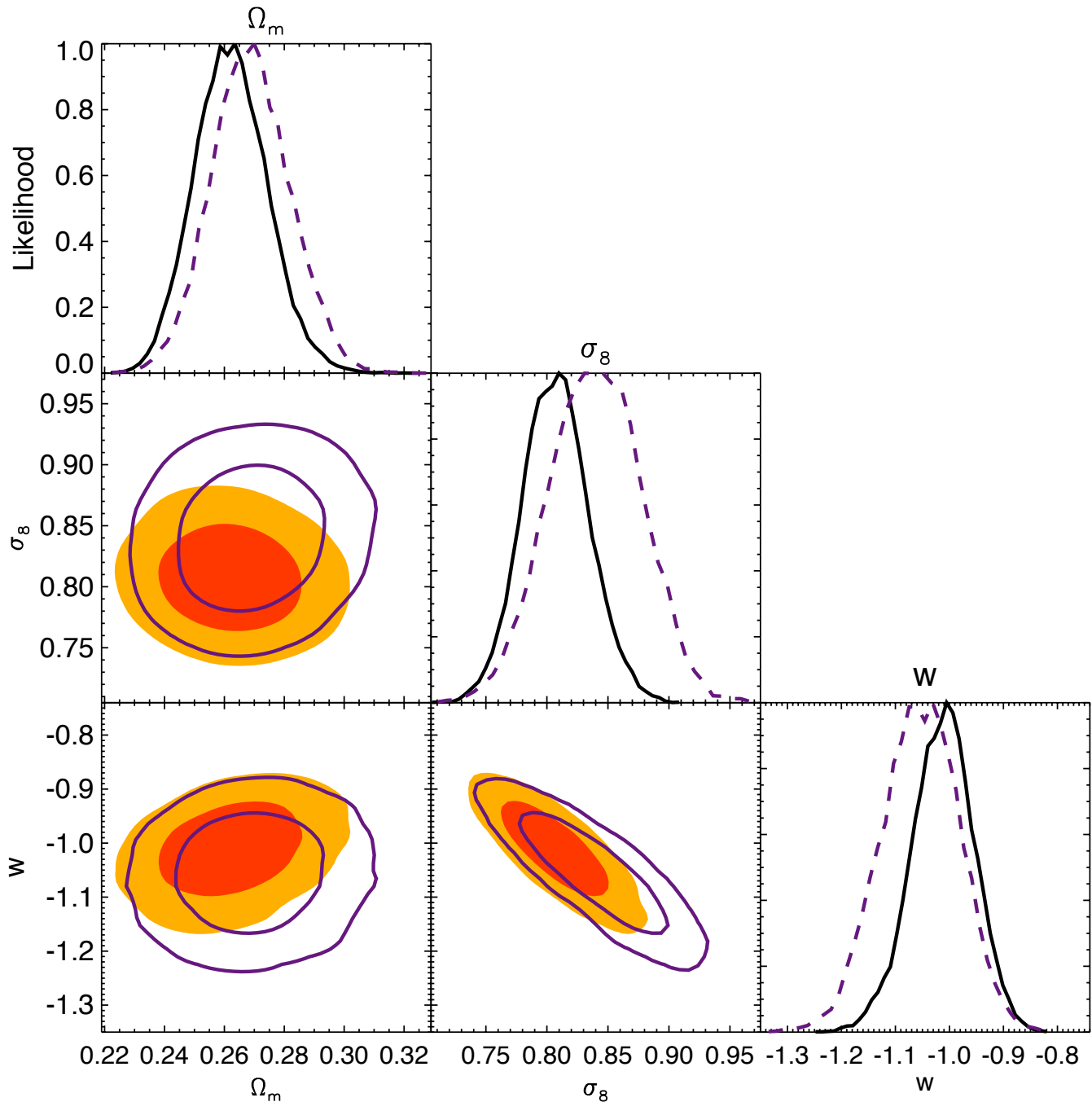


FIG. 6.— Assuming a  $w$ CDM cosmology, the constraints on  $\Omega_m$ ,  $\sigma_8$ , and  $w$ . The plots along the diagonal are the one-dimensional marginalized likelihood. The off-diagonal plots are the two-dimensional marginalized constraints showing the 68% and 95% confidence regions. We show the constraints for the CMB + BAO +  $H_0$  + SNe (purple line contours and dashed lines), and CMB + BAO +  $H_0$  + SNe + SPT<sub>CL</sub> (filled contours and black, solid lines) data sets. Including the SPT<sub>CL</sub> data improves the constraints on  $\Omega_m$ ,  $\sigma_8$ , and  $w$  by factors of 1.1, 1.4, and 1.3 respectively.

lensing observations of  $\sim 35$  SPT-detected clusters spanning  $0.30 < z < 1.3$  using the Magellan and *Hubble* telescopes. Third, we have been awarded time for optical velocity dispersion observations of  $\sim 100$  SPT-detected clusters using the Very Large Telescope (VLT) and a large NOAO program on Gemini South. Fourth, the DES will also yield weak lensing mass estimates ( $S/N \sim 1$ ) of all SPT cluster candidates. The combination of the X-ray, velocity dispersion, and weak lensing obser-

vations will enable valuable cross-checks between these different mass estimates and should lead to significant improvements in the cluster mass calibration.

## 8. CONCLUSIONS

We have presented a catalog of 224 cluster candidates detected with signal-to-noise greater than 4.5 in 720 deg<sup>2</sup> of the SPT survey. Using optical/NIR follow-up data, we have detected clear counterparts for 158 of these candidates, of which 135 were first identified as galaxy clus-



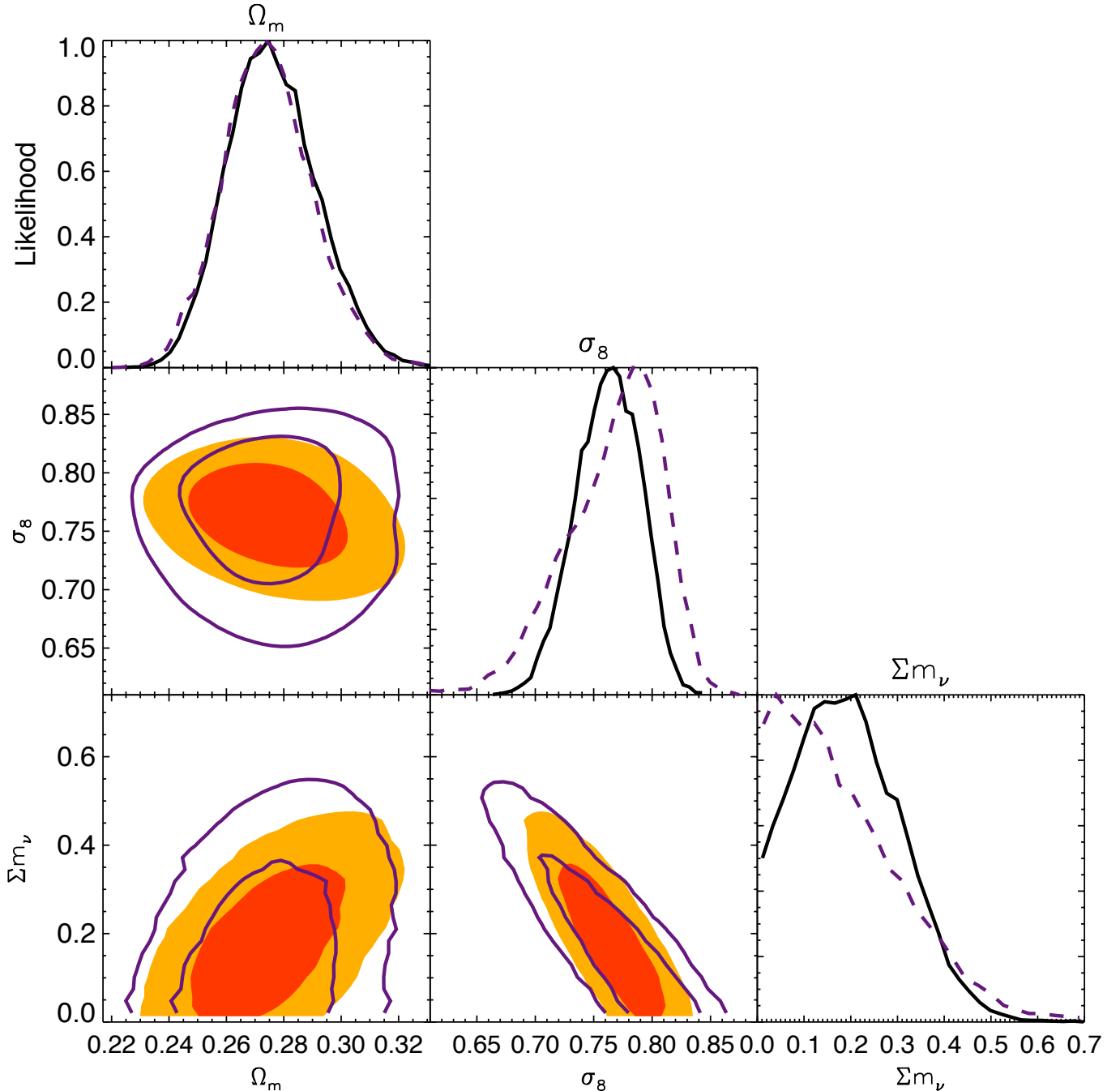


FIG. 7.— Assuming a  $\Lambda$ CDM + massive neutrino cosmology, the constraints on  $\Omega_m$ ,  $\sigma_8$ , and  $\Sigma m_\nu$ . The plots along the diagonal are the one-dimensional marginalized likelihood. The off-diagonal plots are the two-dimensional marginalized constraints showing the 68% and 95% confidence regions. We show the constraints for the CMB + BAO +  $H_0$  (purple line contours and dashed lines), and CMB + BAO +  $H_0$  + SPT<sub>CL</sub> (filled contours and black, solid lines) data sets. The SPT<sub>CL</sub> data leads to a small preference for positive neutrino masses with  $\Sigma m_\nu = 0.17 \pm 0.13$  eV; the 95% CL upper limit on the neutrino masses is reduced from  $\Sigma m_\nu < 0.44$  eV to  $\Sigma m_\nu < 0.38$  eV.

ters in the SPT data. The observed purity of the full sample is 71%; the purity rises to 95% for the 121 candidates detected at a signal-to-noise greater than 5. We report photometric and in some cases spectroscopic redshifts for these galaxy clusters, finding redshifts between  $0.0552 < z < 1.37$  with a median redshift of  $z = 0.55$ . We also estimate the masses based on simulations and X-ray observations, and find the median mass of the sample is  $M_{500} = 3.3 \times 10^{14} M_\odot h_{70}^{-1}$ . This catalog expands

the total number of published, optically confirmed galaxy clusters discovered with the SPT to 144 and triples the total number of SZ-identified galaxy clusters.

We extend the cosmological fitting algorithm for SZ clusters presented by V10 and B11 in two ways. First, we implement an improved treatment of unconfirmed cluster candidates. This improvement has minimal impact given the high purity ( $\sim 95\%$ ) of the  $\xi > 5$  catalog. Second and more importantly, we develop a framework for

combining cluster counts from fields observed with different noise levels, using simulations to recalibrate the SZ detection significance in each field. This framework will be essential for optimally analyzing the final SPT catalog.

We derive cosmological constraints based on the measured cluster abundances. In these analyses, we limit the cluster sample to the 100 cluster candidates detected with signal-to-noise  $\xi > 5$  and  $z > 0.3$  (or optically-unconfirmed). Using just the information from these clusters and a BBN +  $H_0$  prior, we see a sizeable improvement to the constraints on a  $\Lambda$ CDM cosmological model compared to the constraints reported in B11 with a smaller cluster sample and similar priors. However, when additional data (CMB + BAO + SNe) are added, the constraints from the cluster sample presented here are similar to those from B11. This is to be expected, because the B11 constraints were already limited by mass calibration uncertainty, not cluster sample size.

Adding the SPT cluster data to CMB+BAO+ $H_0$ +SNe data constrains the equation of state of dark energy to be  $w = -1.010 \pm 0.058$ . The uncertainty is a factor of 1.3 smaller than that without the SPT catalog and the preferred value remains consistent with a cosmological constant. The addition of SPT cluster data also reduces the uncertainty on  $\sigma_8$  in a  $w$ CDM cosmology by a factor of 1.4 from  $\sigma_8 = 0.840 \pm 0.038$  to  $\sigma_8 = 0.807 \pm 0.027$ .

We also use the measured SZ cluster counts to constrain  $\sigma_8$  and the sum of the neutrino masses. In an extension to the  $\Lambda$ CDM model that includes massive neutrinos, the SZ cluster counts tighten the  $\sigma_8$  constraint by a factor of 1.4 when added to the CMB+BAO+ $H_0$  data. This leads to a small preference for positive neutrino masses with  $\sum m_\nu = 0.17 \pm 0.13$  eV. The 95% confidence upper limit on the total neutrino mass slightly decreases from 0.44 eV to 0.38 eV. The relative improvement to the upper limit is less than would be expected because of the preference for higher neutrino masses.

The SPT survey of 2500 deg<sup>2</sup> was completed in November, 2011. The survey area, comprising 6% of the total sky, has been mapped to depths of approximately 40, 18, and 70  $\mu$ K<sub>CMB</sub>-arcmin at 95, 150, and 220 GHz respectively. These depths are roughly equal to those of the 2009 data presented here. The survey should detect  $\sim 550$  optically-confirmed galaxy clusters at signal-to-noise  $\xi > 4.5$ , with a median redshift of  $\sim 0.5$  and a median mass of  $M_{500} \sim 3 \times 10^{14} M_\odot h_{70}^{-1}$ . Ongoing X-ray, weak lensing, and optical velocity dispersion observations of SPT SZ-selected clusters will be used to produce an improved cluster mass calibration of the sample. The full SPT survey and improved mass calibration will lead to constraints on the dark energy equation of state,  $w$ , better than current constraints from the combination of CMB+BAO+SNe data and will provide an independent systematic test of the standard dark energy paradigm by measuring the effect of dark energy on the growth of structure. Furthermore, the combination of CMB+BAO+SNe constraints with those from the full SPT cluster sample will break parameter degeneracies that exist in either data set alone, resulting in significantly tighter constraints on dark energy. The addition of the SPT cluster abundance data is also already leading to tighter constraints on the sum of the neutrino masses;

with the ongoing program to improve the cluster mass calibration, it may be possible to produce a significant detection of non-zero neutrino mass.

The South Pole Telescope program is supported by the National Science Foundation through grant ANT-0638937. Partial support is also provided by the NSF Physics Frontier Center grant PHY-0114422 to the Kavli Institute of Cosmological Physics at the University of Chicago, the Kavli Foundation, and the Gordon and Betty Moore Foundation. Galaxy cluster research at Harvard is supported by NSF grant AST-1009012. Galaxy cluster research at SAO is supported in part by NSF grants AST-1009649 and MRI-0723073. The McGill group acknowledges funding from the National Sciences and Engineering Research Council of Canada, Canada Research Chairs program, and the Canadian Institute for Advanced Research. X-ray research at the CfA is supported through NASA Contract NAS 8-03060. This work is based in part on observations made with the Spitzer Space Telescope, which is operated by the Jet Propulsion Laboratory, California Institute of Technology under a contract with NASA. Support for this work was provided by NASA through an award issued by JPL/Caltech. The Munich group acknowledges support from the Excellence Cluster Universe and the DFG research program TR33. R.J.F. is supported by a Clay Fellowship. B.A.B is supported by a KICP Fellowship, M.Bautz acknowledges support from contract 2834-MIT-SAO-4018 from the Pennsylvania State University to the Massachusetts Institute of Technology. M.D. acknowledges support from an Alfred P. Sloan Research Fellowship, W.F. and C.J. acknowledge support from the Smithsonian Institution, and B.S. acknowledges support from the Brinson Foundation.

Support for X-ray analysis was provided by NASA through Chandra Award Numbers 12800071, 12800088, and G02-13006A issued by the Chandra X-ray Observatory Center, which is operated by the Smithsonian Astrophysical Observatory for and on behalf of NASA under contract NAS8-03060. Optical imaging data from the Blanco 4 m at Cerro Tololo Interamerican Observatories (programs 2005B-0043, 2009B-0400, 2010A-0441, 2010B-0598) and spectroscopic observations from VLT programs 086.A-0741 and 286.A-5021 and Gemini program GS-2009B-Q-16 were included in this work. Additional data were obtained with the 6.5 m Magellan Telescopes located at the Las Campanas Observatory, Chile.

We acknowledge the use of the Legacy Archive for Microwave Background Data Analysis (LAMBDA). Support for LAMBDA is provided by the NASA Office of Space Science. This research used resources of the National Energy Research Scientific Computing Center, which is supported by the Office of Science of the U.S. Department of Energy under Contract No. DE-AC02-05CH11231. This research has made use of the SIMBAD database, operated at CDS, Strasbourg, France, and the NASA/IPAC Extragalactic Database (NED) which is operated by the Jet Propulsion Laboratory, California Institute of Technology, under contract with the National Aeronautics and Space Administration.

*Facilities:* Blanco (MOSAIC, NEWFIRM), CXO (ACIS), Gemini-S (GMOS), Magellan:Baade (IMACS),

## REFERENCES

- Abell, G. O., Corwin, Jr., H. G., & Olowin, R. P. 1989, *ApJS*, 70, 1
- Ahmad, Q. R., et al. 2002, *Phys. Rev. Lett.*, 89, 011301
- Allen, S. W., Evrard, A. E., & Mantz, A. B. 2011, *ARA&A*, 49, 409
- Amanullah, R., et al. 2010, *ApJ*, 716, 712
- Andersson, K., et al. 2011, *ApJ*, 738, 48
- Ashby, M. L. N., et al. 2009, *ApJ*, 701, 428
- Ashie, Y., et al. 2004, *Phys. Rev. Lett.*, 93, 101801
- Barbosa, D., Bartlett, J., Blanchard, A., & Oukbir, J. 1996, *A&A*, 314, 13
- Battye, R. A., & Weller, J. 2003, *Phys. Rev. D*, 68, 083506
- Beers, T. C., Flynn, K., & Gebhardt, K. 1990, *AJ*, 100, 32
- Benson, B. A., et al. 2011, *ArXiv e-prints*
- Böhringer, H., et al. 2004, *A&A*, 425, 367
- Brodwin, M., et al. 2010, *ApJ*, 721, 90
- Buckley-Geer, E. J., et al. 2011, *ApJ*, 742, 48
- Carlstrom, J. E., Holder, G. P., & Reese, E. D. 2002, *ARA&A*, 40, 643
- Carlstrom, J. E., et al. 2011, *PASP*, 123, 568
- Cash, W. 1979, *ApJ*, 228, 939
- Cavaliere, A., & Fusco-Femiano, R. 1976, *A&A*, 49, 137
- Collister, A. A., & Lahav, O. 2004, *PASP*, 116, 345
- Dalton, G. B., Efstathiou, G., Maddox, S. J., & Sutherland, W. J. 1994, *MNRAS*, 269, 151
- Dalton, G. B., Maddox, S. J., Sutherland, W. J., & Efstathiou, G. 1997, *MNRAS*, 289, 263
- de Grandi, S., et al. 1999, *ApJ*, 514, 148
- de Zotti, G., Ricci, R., Mesa, D., Silva, L., Mazzotta, P., Toffolatti, L., & González-Nuevo, J. 2005, *A&A*, 431, 893
- Desai, S., et al. 2011, in *Bulletin of the American Astronomical Society*, Vol. 43, American Astronomical Society Meeting Abstracts #217, 334.03
- Duus, A., & Newell, B. 1977, *ApJS*, 35, 209
- Ebeling, H., Voges, W., Böhringer, H., Edge, A. C., Huchra, J. P., & Briel, U. G. 1996, *MNRAS*, 281, 799
- Eguchi, K., et al. 2003, *Physical Review Letters*, 90, 021802
- Eikenberry, S., et al. 2006, in *Society of Photo-Optical Instrumentation Engineers (SPIE) Conference Series*, Vol. 6269, Society of Photo-Optical Instrumentation Engineers (SPIE) Conference Series
- Feitsova, T. S. 1981, *Soviet Ast.*, 25, 647
- Foley, R. J., et al. 2011, *ApJ*, 731, 86
- Haiman, Z., Mohr, J. J., & Holder, G. P. 2001, *ApJ*, 553, 545
- Hamann, J., Lesgourgues, J., & Mangano, G. 2008, *JCAP*, 3, 4
- High, F. W., et al. 2010, *ApJ*, 723, 1736
- Holder, G., Haiman, Z., & Mohr, J. J. 2001, *ApJ*, 560, L111
- Holder, G. P., & Carlstrom, J. E. 2001, *ApJ*, 558, 515
- Kalberla, P., Burton, W., Hartmann, D., Arnal, E., Bajaja, E., Morras, R., & Pöppel, W. 2005, *A&A*, 440, 775
- Keisler, R., et al. 2011, *ApJ*, 743, 28
- Kirkman, D., Tytler, D., Suzuki, N., O'Meara, J. M., & Lubin, D. 2003, *ApJS*, 149, 1
- Komatsu, E., et al. 2011, *ApJS*, 192, 18
- Lewis, A., & Bridle, S. 2002, *Phys. Rev. D*, 66, 103511
- Lewis, A., Challinor, A., & Lasenby, A. 2000, *ApJ*, 538, 473
- Lima, M., & Hu, W. 2007, *Phys. Rev. D*, 76, 123013
- Lueker, M., et al. 2010, *ApJ*, 719, 1045
- Mantz, A., Allen, S. W., Ebeling, H., Rapetti, D., & Drlica-Wagner, A. 2010, *MNRAS*, 406, 1773
- Marriage, T. A., et al. 2011, *ApJ*, 737, 61
- Melin, J.-B., Bartlett, J. G., & Delabrouille, J. 2006, *A&A*, 459, 341
- Menanteau, F., et al. 2010, *ApJS*, 191, 340
- Miknaitis, G., et al. 2007, *ApJ*, 666, 674
- Mohr, J. J., et al. 2008, in *Society of Photo-Optical Instrumentation Engineers (SPIE) Conference Series*, Vol. 7016, Society of Photo-Optical Instrumentation Engineers (SPIE) Conference Series
- Molnar, S. M., Haiman, Z., Birkinshaw, M., & Mushotzky, R. F. 2004, *ApJ*, 601, 22
- Montroy et al. 2012, In prep.
- Motl, P. M., Hallman, E. J., Burns, J. O., & Norman, M. L. 2005, *ApJ*, 623, L63
- Murphy, T., et al. 2010, *MNRAS*, 402, 2403
- Padin, S., et al. 2008, *Appl. Opt.*, 47, 4418
- Papovich, C. 2008, *ApJ*, 676, 206
- Percival, W. J., et al. 2010, *MNRAS*, 401, 2148
- Perlmutter, S., et al. 1999, *ApJ*, 517, 565
- Piffaretti, R., Arnaud, M., Pratt, G. W., Pointecouteau, E., & Melin, J.-B. 2011, *A&A*, 534, A109
- Planck Collaboration et al. 2011, *A&A*, 536, A8
- Quintana, H., & White, R. A. 1990, *Ap&SS*, 173, 265
- Reichardt, C. L., et al. 2011, *ArXiv e-prints*
- Rest, A., et al. 2005, *ApJ*, 634, 1103
- Riess, A. G., et al. 1998, *AJ*, 116, 1009
- Riess, A. G., et al. 2011, *ApJ*, 730, 119
- Rozo, E., et al. 2010, *ApJ*, 708, 645
- Ruhl, J., et al. 2004, in *Proc. SPIE*, Vol. 5498, Millimeter and Submillimeter Detectors for Astronomy II, ed. J. Zmuidzinas, W. S. Holland, & S. Withington (Bellingham: SPIE Optical Engineering Press), 11–29
- Saliwanchik et al. 2012, In prep.
- Schaffer, K. K., et al. 2011, *ApJ*, 743, 90
- Sehgal, N., Bode, P., Das, S., Hernandez-Monteagudo, C., Huffenberger, K., Lin, Y., Ostriker, J. P., & Trac, H. 2010, *ApJ*, 709, 920
- Sérsic, J. L. 1974, *Ap&SS*, 28, 365
- Shaw, L. D., Nagai, D., Bhattacharya, S., & Lau, E. T. 2010, *ApJ*, 725, 1452
- Shimon, M., Sadeh, S., & Rephaeli, Y. 2011, *MNRAS*, 412, 1895
- Shirokoff, E., et al. 2011, *ApJ*, 736, 61
- Song, J., A. & B. 2012a, In prep
- Song, J., Mohr, J. J., Barkhouse, W. A., Warren, M. S., & Rude, C. 2012b, *ApJ*, 747, 58
- Staniszewski, Z., et al. 2009, *ApJ*, 701, 32
- Stern, D., et al. 2005, *ApJ*, 631, 163
- Story, K., et al. 2011, *ApJ*, 735, L36+
- Struble, M. F., & Rood, H. J. 1999, *ApJS*, 125, 35
- Sunyaev, R. A., & Zel'dovich, Y. B. 1972, *Comments on Astrophysics and Space Physics*, 4, 173
- Tinker, J., Kravtsov, A. V., Klypin, A., Abazajian, K., Warren, M., Yepes, G., Gottlöber, S., & Holz, D. E. 2008, *ApJ*, 688, 709
- Šuhada, R., et al. 2010, *A&A*, 514, L3+
- van Engelen, A., et al. 2012, *ArXiv e-prints*
- Vanderlinde, K., et al. 2010, *ApJ*, 722, 1180
- Vieira, J. D., et al. 2010, *ApJ*, 719, 763
- Vikhlinin, A., et al. 2009a, *ApJ*, 692, 1033
- . 2009b, *ApJ*, 692, 1060
- Voges, W., et al. 1999, *A&A*, 349, 389
- . 2000, *VizieR Online Data Catalog*, 9029, 0
- Wang, L., & Steinhardt, P. J. 1998, *ApJ*, 508, 483
- Wang, S., Haiman, Z., Hu, W., Khoury, J., & May, M. 2005, *Physical Review Letters*, 95, 011302
- Wang, S., Khoury, J., Haiman, Z., & May, M. 2004, *Phys. Rev. D*, 70, 123008
- Williamson, R., et al. 2011, *ApJ*, 738, 139

## APPENDIX







TABLE 6 — *Continued*

ID & coordinates:			$Y_{SZ} \times 10^6$ (arcmin <sup>2</sup> )	Significances			Best		Redshift	$M_{500}$ ( $10^{14} h_{70}^{-1} M_{\odot}$ )
SPT ID	RA	DEC		$\theta_c=0.5'$	1.5'	2.5'	$\xi$	$\theta_c$		
SPT-CL J2152-5143	328.0034	-51.7245	67 ± 24	4.45	4.33	3.79	4.53	0.75	0.40 ± 0.03	2.82 ± 0.96
SPT-CL J2152-5633	328.1458	-56.5641	100 ± 21	5.16	5.66	5.68	5.84	1.75	> 1.50 <sup>A</sup>	-
SPT-CL J2155-5103	328.8747	-51.0508	73 ± 25	4.11	4.41	4.40	4.52	1.75	> 1.06 <sup>A</sup>	-
SPT-CL J2155-5225	328.8941	-52.4169	95 ± 25	4.45	4.77	4.36	4.77	1.50	0.59 ± 0.04	2.86 ± 0.93
SPT-CL J2155-6048	328.9851	-60.8072	88 ± 20	4.87	5.19	4.56	5.24	1.00	0.5390	2.93 ± 0.79
SPT-CL J2158-4702	329.6901	-47.0348	78 ± 23	4.50	4.38	4.17	4.56	1.00	> 0.90 <sup>A</sup>	-
SPT-CL J2158-4851	329.5737	-48.8536	80 ± 23	4.28	3.38	2.20	4.61	0.25	> 0.75 <sup>A</sup>	-
SPT-CL J2158-5615	329.5975	-56.2588	88 ± 20	4.28	4.42	3.93	4.54	1.25	> 1.07 <sup>A</sup>	-
SPT-CL J2158-6319	329.6390	-63.3175	62 ± 19	4.33	3.43	2.64	4.54	0.25	> 1.06 <sup>A</sup>	-
SPT-CL J2159-6244	329.9922	-62.7420	108 ± 21	6.02	5.98	5.54	6.08	1.00	0.42 ± 0.02	3.57 ± 0.86
SPT-CL J2200-5547	330.0304	-55.7954	79 ± 21	3.83	4.63	4.72	4.80	2.00	> 0.98 <sup>A</sup>	-
SPT-CL J2201-5956	330.4727	-59.9473	338 ± 25	11.61	13.57	13.99	13.99	2.50	0.0972	7.68 ± 1.54
SPT-CL J2202-5936	330.5483	-59.6021	76 ± 19	4.81	4.21	3.36	4.89	0.25	0.46 ± 0.03	2.75 ± 0.82
SPT-CL J2259-5432	344.9820	-54.5356	135 ± 38	4.56	4.71	4.65	4.78	2.00	0.44 ± 0.04	3.18 ± 1.04
SPT-CL J2259-5617	344.9974	-56.2877	99 ± 24	5.04	4.27	3.55	5.29	0.25	0.17 ± 0.02	3.86 ± 1.07
SPT-CL J2300-5331	345.1765	-53.5170	119 ± 27	5.24	5.02	4.65	5.29	0.25	0.2620	3.79 ± 1.00
SPT-CL J2301-5046	345.4585	-50.7823	92 ± 24	4.58	3.83	2.82	4.58	0.50	> 1.50 <sup>A</sup>	-
SPT-CL J2301-5546	345.4688	-55.7758	106 ± 25	5.19	4.93	4.62	5.19	0.50	0.7480	3.21 ± 0.93
SPT-CL J2302-5225	345.6464	-52.4329	104 ± 29	3.77	4.24	4.60	4.60	2.50	> 1.04 <sup>A</sup>	-
SPT-CL J2311-5011	347.8427	-50.1838	91 ± 29	3.40	3.85	4.42	4.64	3.00	> 1.50 <sup>A</sup>	-
SPT-CL J2312-5820	348.0002	-58.3419	89 ± 24	4.66	3.75	3.11	4.78	0.25	0.88 ± 0.09	2.79 ± 0.93
SPT-CL J2329-5831	352.4760	-58.5238	107 ± 25	4.95	4.64	3.96	4.95	0.50	0.82 ± 0.04	2.96 ± 0.96
SPT-CL J2331-5051*	352.9584	-50.8641	166 ± 23	7.86	6.60	5.14	8.04	0.25	0.5760	5.14 ± 0.71
SPT-CL J2332-5358*	353.1040	-53.9733	193 ± 31	7.25	7.30	6.84	7.30	1.50	0.4020	6.54 ± 0.82
SPT-CL J2334-5953	353.6989	-59.8892	94 ± 30	2.94	3.98	4.53	4.53	2.50	> 1.50 <sup>A</sup>	-
SPT-CL J2337-5942*	354.3544	-59.7052	312 ± 24	14.72	12.63	10.11	14.94	0.25	0.7750	8.21 ± 1.14
SPT-CL J2341-5119*	355.2994	-51.3328	227 ± 24	9.48	9.02	7.74	9.65	0.75	1.0030	5.61 ± 0.82
SPT-CL J2342-5411*	355.6903	-54.1887	132 ± 23	6.18	5.24	3.96	6.18	0.50	1.0750	3.00 ± 0.50
SPT-CL J2343-5521	355.7574	-55.3641	130 ± 28	4.87	5.58	5.74	5.74	2.50	> 1.50 <sup>A</sup>	-
SPT-CL J2343-5556	355.9290	-55.9371	106 ± 27	4.49	4.53	4.00	4.58	1.00	> 1.21 <sup>A</sup>	-
SPT-CL J2351-5452	357.8877	-54.8753	151 ± 47	4.35	4.70	4.83	4.89	2.75	0.3838	3.32 ± 1.04
SPT-CL J2355-5056*	358.9551	-50.9367	138 ± 24	5.73	5.34	4.31	5.89	0.75	0.3196	4.11 ± 0.54
SPT-CL J2359-5009*	359.9208	-50.1600	152 ± 27	6.19	6.23	5.64	6.35	1.25	0.7750	3.57 ± 0.57

NOTE. — Galaxy cluster candidates selected above a significance of 4.5 in the first 720 deg<sup>2</sup> of the SPT survey. Galaxy clusters marked by a ‘\*’ have X-ray data that are used in the cosmological analysis (see A11 and B11 for a description of the X-ray data). For each candidate, we report the detection significance of each candidate in the ‘Best’ column, as well as the significances at a fixed set of three core radii (§3). We also report the position and (if confirmed) redshift (§4). Spectroscopic redshifts are quoted without uncertainties. The integrated  $Y_{SZ}$  is reported for a 1’ aperture (§3.3). Finally, we report a mass estimate for each confirmed cluster marginalized over the  $\Lambda$ CDM chain (§7.1.2).

<sup>A</sup> Unconfirmed cluster candidate which is either above the quoted redshift limit or a false detection.